



How spice is stirred in the Bay of Bengal

G. Spiro Jaeger*

Massachusetts Institute of Technology, Cambridge, MA, USA

Woods Hole Oceanographic Institution, Woods Hole, MA, USA

J. MacKinnon and A. Lucas

Scripps Institution of Oceanography, La Jolla, CA, USA

E. Shroyer and J. Nash

Oregon State University, Corvallis, OR, USA

A. Tandon

University of Massachusetts Dartmouth, North Dartmouth, MA, USA

J.T. Farrar and A. Mahadevan

Woods Hole Oceanographic Institution, Woods Hole, MA, USA

*Corresponding author address: Woods Hole Oceanographic Institution, Woods Hole, MA, USA

E-mail: gvsj@alum.mit.edu

ABSTRACT

15 The scale-dependent variance of tracer properties in the ocean bears the im-
16 print of the oceanic eddy field. Anomalies in spice (which combines anom-
17 alies in temperature (T) and salinity (S) on isopycnal surfaces) act as passive
18 tracers beneath the surface mixed layer (ML). We present an analysis of spice
19 distributions along isopycnals in the upper 200 m of the ocean, calculated with
20 over 9000 vertical profiles of T and S measured along \sim 4800 km of ship tracks
21 in the Bay of Bengal. The data are from three separate research cruises – in
22 the winter monsoon season of 2013, and in the late and early summer mon-
23 soon seasons of 2015 and 2018. We present a spectral analysis of horizontal
24 tracer variance statistics on scales ranging from the submesoscale (\sim 1 km)
25 to the mesoscale (\sim 100 km). Isopycnal layers that are closer to the ML-base
26 exhibit redder spectra of tracer variance at scales \lesssim 10 km than is predicted
27 by theories of quasi-geostrophic turbulence or frontogenesis. Two plausible
28 explanations are postulated. The first is that stirring by submesoscale motions
29 and shear dispersion by near-inertial waves enhance effective horizontal mix-
30 ing and deplete tracer variance at horizontal scales \lesssim 10 km in this region.
31 The second is that the spice anomalies are coherent with dynamical properties
32 such as potential vorticity, and not interpretable as passively stirred.

33 **1. Introduction**

34 The stirring and mixing of properties by the oceanic flow field is of longstanding interest for
35 understanding the dispersal and distribution of substances such as heat, salt, dissolved gases, nu-
36 trients, phytoplankton, and pollutants. Conversely, the patterns of chemical and physical tracer
37 distributions in the ocean can be used to interpret the dynamical characteristics of the flow. Within
38 the vast range of spatial scales on which ocean currents and eddying motions act to stir properties,
39 the submesoscale, and related dynamics, remain difficult to observe.

40 Submesoscale processes manifest at spatial scales $O(1\text{--}10)$ km, have timescales comparable to
41 near-inertial waves, and play a key role in the vertical transport of properties, such as nutrients and
42 buoyancy (Lévy et al. 2012; Thomas et al. 2008). They also facilitate the downscale cascade of
43 energy through the loss of balance of mesoscale flows (Capet et al. 2008), thereby connecting the
44 larger $O(100)$ km mesoscale with the smaller (<10 m) dissipative scales. Observations of ther-
45 mohaline compensation (Rudnick and Martin 2002), vorticity and divergence (Shcherbina et al.
46 2015), and the dispersion of drifters at fronts (D'Asaro et al. 2018; Essink et al. 2019), have shown
47 the key role of submesoscale dynamics in controlling horizontal stirring and mixing within the
48 surface mixed layer. But, below the surface mixed layer, in what is classically considered the inte-
49 rior domain of isopycnal stirring, the role of submesoscale dynamics and forward energy cascades
50 remains unclear (McWilliams 2016). Here, the effect of a downscale kinetic energy transfer on
51 tracer variance, though seen in models of the submesoscale dynamical regime (Badin et al. 2011),
52 has not been observed in the ocean.

53 Measurements of submesoscale dynamics have been stymied by the difficulty of synoptically
54 observing a three-dimensional flow field in an area that is tens of kilometers wide, while resolving
55 features that are a kilometer or sub-kilometer in extent and evolving on time scales of $O(1$ day).

56 Additionally, the kinetic and potential energy of such flows is dominated by internal gravity waves
57 that mask the signal of vortical submesoscale dynamics (Callies and Ferrari 2013). Vortical mo-
58 tions are associated with anomalies in Ertel potential vorticity and evolve on time scales that
59 range from sub-inertial to inertial. While recent studies have made progress in observing their
60 submesoscale signatures (Thompson et al. 2016), challenges remain in directly measuring the
61 submesoscale flow fields, which are responsible for stirring tracers. Oceanographers have instead
62 examined the variability of tracer fields on isopycnal surfaces to infer the underlying dynamics
63 (Kunze et al. 2015; Klymak et al. 2015).

64 We present a new look at along-isopycnal tracer variability on scales ranging from 1–100 km,
65 from a synthesis of data collected during three research cruises in the Bay of Bengal (BoB). This
66 large basin in the northern Indian Ocean has the following characteristics: (i) It is strongly stratified
67 in the upper 50 m by freshwater inputs, (ii) it contains distinct water masses, and hence, large-
68 scale gradients of spice, a passive tracer, (iii) it hosts energetic eddies, and (iv) it is forced by both
69 consistent winds and impulsive storms. It is thus a prime location for studying the dynamics of the
70 upper ocean, both within the highly stratified pycnocline layers at the base of the mixed layer, and
71 within the weaker pycnocline beneath.

72 Our analysis of these new observations of water mass distributions in the BoB reveals statistics
73 inconsistent with existing descriptions of tracer stirring in the stratified ocean. The observed tracer
74 gradient distributions within the shallow stratified pycnocline do not support quasi-geostrophic
75 or ageostrophic theories of homogeneous turbulence. The relative paucity of tracer variance be-
76 low 10 km scales compared to larger scales in our observations cannot be easily explained. We
77 speculate that, most likely, submesoscale motions play a more important role than was previously
78 envisaged in stirring tracer and dissipating its variance in the ocean’s near-surface interior, as has
79 also been suggested by other studies recently Yu et al. (2019); Siegelman et al. (2020).

80 In an accompanying study (Jaeger et al. 2019), we analyzed layered features in spice anomaly
81 (water mass contrast) in the BoB and explained their formation by submesoscale processes. Here,
82 we present the statistics of scale-dependent spice variance along isopycnal surfaces, which to a
83 large extent, omits the effect of internal waves and is therefore viewed as a signature of along-
84 isopycnal stirring. The relation between the layered intrusions of spice and along-isopycnal vari-
85 ance is discussed in Jaeger (2019).

86 In what follows, we begin by reviewing theories of ocean stirring (Section 2). We then describe
87 our new observations, with some details about the instruments and measurements in Section 3. Our
88 methods for parsing through the ship sections and constructing spectra of along-isopycnal tracer
89 variance are described in Section 4, and our statistical results are presented in Section 5. In order
90 to provide context to our findings we compare the spectra calculated in the BoB to those from the
91 Pacific and Atlantic Oceans (Section 6), and provide potential explanations for the differences. We
92 provide brief conclusions in Section 7. Supplementary figures are included.

93 **2. Oceanic Variance Spectra**

94 Tracer gradients exist across a wide range of spatial scales in the ocean, from thousands of
95 kilometers down to millimeters, and are connected by a down-scale variance cascade (Smith and
96 Ferrari 2009). Gradients are stirred, strained, and sharpened by motions ranging from the ocean
97 gyres, eddies, and internal waves, to small enough scales where three-dimensional turbulence and
98 molecular diffusion ultimately mix properties (Shcherbina et al. 2015). The large-scale currents,
99 with scales $O(10)$ km or more, are described by balanced sub-inertial quasi-geostrophic (QG) dy-
100 namics, which exhibits an upscale transfer of energy. At the smallest scales of $O(10)$ m in the
101 ocean interior, shear instabilities and breaking internal waves produce isotropic turbulence that
102 effectively mixes tracers and erases tracer gradients and variance (MacKinnon et al. 2013). In be-

¹⁰³ tween these scales, in the regime of submesoscale dynamics, wave dynamics, frontal instabilities,
¹⁰⁴ and vorticity containing modes are relevant (Polzin and Ferrari 2004; McWilliams 2016).

¹⁰⁵ The typical scales of the motions stirring the ocean determine the distribution of the typical
¹⁰⁶ scales of tracer variance. The statistical distribution of tracer variance across these scales can be
¹⁰⁷ quantified by a spectral power decomposition (\mathcal{P}_k) as a function of horizontal wavenumber k ,
¹⁰⁸ providing a check on theories that attempt to describe the fluid dynamics, and a way to test the
¹⁰⁹ relative importance of QG and submesoscale dynamics in stirring the ocean. Unlike theoretical
¹¹⁰ studies, observational studies often plot tracer variance spectra as gradient spectra \mathcal{G}_k (multiplying
¹¹¹ \mathcal{P}_k by $4\pi^2 k^2$), either because gradients are the directly measured quantity, or to be able to visually
¹¹² distinguish between variance spectral slopes more easily. We follow this convention, but in the
¹¹³ text, we refer to variance spectra as power laws $\mathcal{P}_k \sim k^m$, and append the whitened gradient
¹¹⁴ spectra power law ($\mathcal{G}_k \sim k^{m+2}$) in parenthesis to avoid misinterpretation.

¹¹⁵ Statistics of tracer patterns relate to statistics of the motions that create those patterns. The fol-
¹¹⁶ lowing descriptions (schematically shown in **Fig.1**) are set in the framework of two-dimensional,
¹¹⁷ homogeneous, stationary macro-turbulence. Making the simplifying assumption for the existence
¹¹⁸ of a turbulent inertial range between the forcing scale (e.g. the baroclinic Rossby radius of defor-
¹¹⁹ mation) and the turbulent dissipation scale, the power spectrum for kinetic energy E_k obeys several
¹²⁰ different power laws. The tracer's variance spectrum \mathcal{P}_k is related to the kinetic energy spectrum
¹²¹ E_k . We offer a brief summary of the tracer variance distributions predicted by different theories of
¹²² ocean dynamics.

¹²³ If $E_k \sim k^{-n}$, then in geostrophic turbulence theory, $\mathcal{P}_k \sim k^{(n-5)/2}$ for $n < 3$ (Callies and Ferrari
¹²⁴ 2013). QG theory for the ocean's interior predicts a kinetic energy spectrum $E_k \sim k^{-3}$ following
¹²⁵ a power law with $n = 3$, and a tracer spectrum $\mathcal{P}_k \sim k^{-1}$ ($\mathcal{G}_k \sim k^{+1}$). If $n > 3$, the the kinetic
¹²⁶ energy spectrum falls off more rapidly, large-scale motions dominate, and the non-local stirring

leads to a Batchelor spectrum, $\mathcal{P}_k \sim k^{-1}$ (Batchelor 1959), equivalent to the interior QG tracer spectrum. Compared to interior QG dynamics, other dynamical theories, summarized below, predict relatively more kinetic energy at smaller scales. Dynamics that are relatively more energetic at smaller scales, stir and eventually mix tracer more efficiently. They lead to relatively less tracer variance at smaller scales as compared to QG dynamics, resulting in the steepening of tracer variance spectra at smaller scales (Callies and Ferrari 2013).

This effect is restricted to the near-surface according to surface-QG (SQG) theory, which predicts steeper tracer spectra of $k^{-5/3}$ (gradient spectra $k^{+1/3}$) near the surface. But, being an extension of interior QG dynamics, the interior-QG spectrum still holds at greater depth, as the surface-enhanced small-scale motions are attenuated with depth (Lapeyre and Klein 2006). On the other hand, stratified turbulence theory also predicts the tracer variance spectrum to be steeper in the ocean's interior following an Obhukov-Corrsin spectrum with $k^{-5/3}$ (gradient spectra $k^{+1/3}$) (Brethouwer and Lindborg 2008). This is ascribed to stirring by turbulent patches with long-and-thin aspect ratios that form, for example, "blinis" or "pancakes" from the geostrophic adjustment of water patches mixed by breaking near-inertial waves (Sundermeyer et al. 2005). Lastly, frontogenesis and ageostrophic dynamics sharpen gradients into fronts more quickly; a series of sharp fronts yields a tracer variance spectrum with a k^{-2} decay, and a flat (k^0) gradient spectrum (Klein et al. 1998).

Even though precise predictions of spectral slopes emerge from the different dynamical theories, their robustness and relevance to actual ocean states is not certain. Theoretical tracer variance distributions are based on assumptions of an inertial range and statistical homogeneity of the flow field, yet it is not clear whether such idealised cascades exist, or whether they are disturbed by flow inhomogeneities such as coherent structures or persistent anisotropic currents, and energy inputs by instabilities across the submesoscale, topographic influence, bottom friction, or atmo-

¹⁵¹ spheric forcing. Nonetheless, existing observational spectral studies (reviewed in the discussion)
¹⁵² make frequent comparisons with the idealised theories, and observational spectra offer insights
¹⁵³ independent of testing predictions.

¹⁵⁴ 3. Observations in the Bay of Bengal

¹⁵⁵ Our study uses hydrographic measurements to calculate statistics of tracer variance, analyzing
¹⁵⁶ the distribution of water mass anomalies. As part of two research programs supported by the U.S.
¹⁵⁷ Office of Naval Research, the Air Sea Interaction Research Initiative (ASIRI) and the ongoing
¹⁵⁸ Monsoon Intra-Seasonal Oscillations in the Bay of Bengal (MISO-BOB), the *R/V Roger Revelle*
¹⁵⁹ and the *R/V Thomas G. Thompson* completed multiple hydrographic surveys of the Bay of Bengal
¹⁶⁰ between 2013 and 2018. Vertical profiles of *T* and *S* were measured to depths of at least 200 m
¹⁶¹ during the ship surveys. Two of the surveys made transects (>100 km) with closely spaced (\leq 300
¹⁶² m) vertical profiles, while one survey completed longer transects (> 500 km) that were sampled
¹⁶³ more coarsely (\leq 5 km spacing between vertical profiles), yielding a total of over 9000 profiles of
¹⁶⁴ *T* and *S*.

¹⁶⁵ a. Environment

¹⁶⁶ The Bay of Bengal's unique hydrographic conditions are linked to the monsoonal circulation
¹⁶⁷ over the northern Indian Ocean, characterized by seasonally reversing winds and intense rainfall
¹⁶⁸ during the summer season. Both rainfall and river runoff contribute freshwater in excess of annual
¹⁶⁹ evaporation from the bay, lowering the surface salinity year-round (Fig.2A), with the lowest values
¹⁷⁰ observed a couple of months after the wet season, when river runoff reaches a maximum (Sengupta
¹⁷¹ et al. 2006). During subsequent winter months when surface cooling would be expected to lower
¹⁷² the surface buoyancy enough to deepen the surface mixed layer, the low salinity of the surface

173 mixed layer inhibits convective mixing and preserves the stratification (Jaeger and Mahadevan
174 2018), maintaining a deep chlorophyll maximum and strong vertical gradient in biogeochemical
175 properties (Lucas et al. 2016; Shroyer et al. 2019). The salinity-stratification limits the depth of
176 wind-forced mixing throughout the year, isolating the sub-surface layers of the Bay of Bengal
177 from direct ventilation (Jinadasa et al. 2016). Seasonal wind-driven upwelling is observed only
178 along the western boundary (Indian coast) during the southwest monsoon (Shetye et al. 1991).

179 Evidence of this persistent insulation is seen in the pronounced oxygen minimum zone below the
180 surface (**Fig. 2B**), which exists even though the Bay of Bengal's surface primary production is not
181 elevated compared to other tropical oceans (supplementary **Fig. S1**). Shown in the same figure,
182 oxygen saturation on a particular density surface (1023 kg m^{-3}) shows a marked along-isopycnal
183 contrast between the Bay of Bengal and the equatorial Indian Ocean to the south, indicating a
184 relative lack of exchange between the basins and a long residence time of water in the interior of
185 the BoB.

186 While ventilation of the interior via direct vertical exchange (wind-driven mixing, upwelling,
187 or buoyancy-loss driven convection) is weak (Prasanna Kumar et al. 2002), recent observational
188 studies show sub-surface eddies (Prasanna Kumar et al. 2004) advected from the Andaman Sea
189 (Sarma and Udaya Bhaskar 2018; Gordon et al. 2017) to be a source of ventilation for the interior
190 Bay of Bengal. Strong internal tides, internal waves, and sub-surface mixing are observed over the
191 shallow topography of the Andaman-Nicobar Submarine Ridge separating the Andaman Sea from
192 the Bay of Bengal (Yi-Neng et al. 2012). The mixing in this region creates a fresher and colder
193 water mass in contrast to the waters in the interior BoB (**Fig. 3**).

194 In addition to enhanced vertical salinity gradients above the thermocline, freshwater forcing
195 also creates horizontal gradients in salinity, filling the BoB with both dynamic fronts in density,
196 and passive (along isopycnal) contrasts between different water masses in the pycnocline (Gordon

197 et al. 2016). Climatological sub-surface isopycnal salinity fields are shown on an isopycnal surface
198 for 3 different annual periods during which in-situ observations were taken (**Fig.3**). The three
199 expeditions took place in three different seasons: southwesterly winds and rain during the early
200 summer and late summer monsoon marked the cruises from June 6 to 18, 2018, and from August
201 24 to September 19, 2015, while dry northeasterly winds of the winter monsoon (and one cyclone)
202 prevailed during the first cruise from November 29 to December 11 2013.

203 The sub-surface salinity fields from MIMOC, the Monthly Isopycnal & Mixed-layer Ocean Cli-
204 matology (Schmidtko et al. 2013), which is based primarily on Argo profiles, reveal the presence
205 of both a salty (and relatively warm) water mass infiltrating from the Arabian Sea, and a fresh (and
206 relatively cold) water mass leaking in from the Andaman Sea through channels in between the
207 chain of Andaman and Nicobar Islands. The monthly climatological fields on the 1023 kg m^{-3}
208 ($\sigma = 23$) density surface exhibit persistent gradients between these end-member water masses.
209 Compared to climatological salinity gradients, synoptic gradients are expected to contain higher
210 variability at mesoscales. Indeed the expeditions sampled substantially fresher and saltier water
211 and sharper gradients than the climatology in the interior of the bay. Mesoscale surface currents
212 during the in-situ observational period (based on AVISO sea surface topography) are dominated
213 by eddies that are $O(100)$ km in horizontal extent.

214 Climatological fields of sub-surface salinity anomalies on isopycnal surfaces (compensated by
215 temperature) display both an east-west gradient within the bay, and a north-south gradient in the
216 southern bay (**Fig.3**). The mean monthly patterns of salinity offer insights into time-mean sub-
217 surface flows, mirroring the spatial distribution of oxygen along this same density surface. Along
218 the $\sigma = 23$ surface at around 70 m depth, the higher salinity of the equatorial Indian Ocean in-
219 filtrates into the Bay of Bengal along its western margin, especially later in the summer. This
220 increases the mean salinity and its gradients in the eastern BoB by winter, at which point the mean

221 flow at the southern edge is southbound again. The meeting of distinct water masses in the upper
222 200 m of the Bay of Bengal make it an interesting site to study the processes affecting lateral tracer
223 transport both within and below highly stratified ocean layers.

224 *b. Measurement of T and S*

225 The 2013 survey used an Oceanscience UCTD Underway Profiling System (or Underway CTD
226 system, or UCTD), measuring seawater conductivity, temperature, and pressure (Ramachandran
227 et al. 2018). The profiler contains a battery-powered, internally recording CTD, attached with a
228 long line to a tail spool. During the long sections while the ship was underway at \sim 8 kn, the
229 UCTD system was deployed in “free cast” mode. The probe is dropped over the stern and falls
230 nearly vertically while unwinding line from its tail spool. On the deck, a winch pays out line
231 to compensate for the ship’s forward travel. Designed to fall through the water at approximately
232 4 m s^{-1} , the probe’s \sim 60 s fall time was set to reach a target depth of at least 200 m for all casts.
233 Round-trip time is considerably longer (\sim 10 min) due to winch recovery and line re-winding time.

234 The 2015 and 2018 surveys used the FCTD system (“Fast” Conductivity Temperature Depth),
235 which was developed at Scripps Institution of Oceanography to collect rapid, real-time CTD pro-
236 files in the upper 2 km of the ocean (Pinkel et al. 2012). The subsurface package is comprised of a
237 streamlined profiler with a Seabird (SBE) 49 CTD and associated telemetry and control electron-
238 ics, affixed to a load-bearing power and signal cable. The profiler is overboarded with a \sim 10 m
239 boom to minimize contamination from the ship’s wake, and retrieved utilizing a custom designed
240 high speed winch. Winch controls are mainly automated, although watch-standers on deck and
241 in the laboratory monitor the system at all times. Real-time CTD and profiler flight dynamics
242 are collected and analyzed continuously. In the BoB, the FCTD was configured to collect pro-
243 files to 200 m depth while the ship was steaming at 4 knots (2015) and 2 knots (2018). Profiler

244 surface-to-surface round-trip time averaged roughly 3 minutes, providing 300 m (or less) horizontal
245 separation between profiles.

246 The UCTD and FCTD profiler's raw measurement of temperature and conductivity at 16 Hz
247 and a fall-rate of approximately 4 and 5 m s⁻¹, yields between 3 to 4 samples per meter in the
248 vertical. Before gridding in depth, salinity was calculated by combining the temperature and
249 conductivity profiles with a small temporal offset based on a lagged-correlation for each profile
250 to eliminate salinity spiking artifacts (Thomson and Emery 2014). A vertically gridded, 1-decibar
251 (approximately 1 m) data product was formed by bin averaging, removing outliers with a median
252 filter, and quality controlling each section, with special attention paid to the small fluctuations
253 in salinity and temperature at depth. In several of the sections, the salinity-spiking correction
254 removes abrupt, step-like horizontal changes in salinity between adjacent sections of profiles.

255 *c. Hydrography of the Upper 200 m*

256 The upper 200 m of the BoB are generally characterized by a shallow halocline transitioning
257 into a deeper thermocline. Representative example profiles of *T*, *S*, and *TS* from each cruise are
258 shown in **Fig.4**, along with the aggregated *TS* profiles from all sections. This thermohaline stratification
259 leads to strong, sharp, and shallow density stratification, defined as the vertical gradient
260 of buoyancy ($N^2 \equiv -\frac{g}{\rho_o} \frac{\partial \rho}{\partial z}$). Average N^2 profiles for each cruise, as well as the spread of density
261 stratification encountered along the isopycnal surfaces $\sigma = 21$ to 26 , are shown in **Fig.5**. Average
262 peak values of $N^2 \sim 3 \times 10^{-3}$ s⁻² (buoyancy frequency $N = 0.04$ s⁻¹) were found at 25 m depth
263 during Aug.-Sep. 2015, and slightly deeper at 50 m during both the Nov.-Dec. 2013 and June
264 2018 surveys.

265 Stratification drops from a peak value of $N^2 \sim 3 \times 10^{-3}$ s⁻² in the sharpest pycnocline layers to
266 10^{-4} s⁻² at 200 m depth. Buoyancy frequency N is typically 100 to 1000 times larger than the local

267 Coriolis frequency $f \sim 3 \times 10^{-5} \text{ s}^{-1}$. The $\sigma = 21$ and 22 isopycnals are on average in the layer
268 of maximum stratification forming the lower boundary of the ML (mean depths approximately
269 40 m and 60 m, mean $N^2 \sim 1 \times 10^{-3} \text{ s}^{-2}$). In 2018 the $\sigma = 22$ isopycnal was always below the
270 peak stratification, while in 2013 and 2015 it sometimes had stronger stratification than the $\sigma =$
271 21 isopycnal above it. The $\sigma = 23, 24, 25$ and 26 isopycnals are always in the interior pycnocline
272 layers (mean depths are 70, 100, 130, 180 m, respectively, mean $N^2 \sim 0.1$ to $0.5 \times 10^{-3} \text{ s}^{-2}$).

273 While at 200 m depth there is very little TS spread across the three different seasons and years,
274 there is considerable along-isopycnal TS spread at intermediate depths between approximately
275 50 –100 m, in between the $\sigma = 22$ and 24 isopycnals. The 2013 survey, which had the largest
276 geographic range, also had the largest range in TS variability along subsurface isopycnals denser
277 than $\sigma = 22$, measuring both the saltiest (warmest) and freshest (coldest) waters compared to water
278 of the same density sampled in the smaller 2015 and 2018 surveys. The smallest TS variability
279 was measured during the 2018 cruise, in which shorter ship tracks were sampled. The surface
280 values show consistent differences between the different seasons. The warmest surface waters
281 were seen in the early summer, the freshest in the later summer monsoon season, and the coldest
282 in the winter season. Most surface mixed layer densities were lighter than $\sigma = 21$, and no surface
283 waters denser than $\sigma = 22$ were encountered.

284 Water mass anomalies are defined as anomalies of absolute salinity S (or conservative tempera-
285 ture T) from the average S (or T) value along isopycnals calculated from all cruises. The salinity
286 anomalies ΔS , scaled by the haline contraction coefficient β , are equivalent to the temperature
287 anomalies ΔT , scaled by the thermal expansion coefficient α , since by definition the anomalies
288 must compensate each other's effect on density. The two components summed together, or equiv-
289 alently, individually multiplied by two, define water mass or "spice" anomalies (Munk 1981). As
290 long as there is a spread in TS values at the same density, water mass variability can be used as a

passive tracer of seawater, since buoyancy gradients and dynamics are not affected by the particular values of T and S , but only their combined effect on density. Though modified at the surface by input (and loss) of freshwater and heat, once subducted beneath the ML, a water parcel's TS properties are conserved as it is stirred on isopycnals, and changed only by interior mixing. Water mass variance forced at large scales cascades to smaller scales and is ultimately dissipated at the 3-D turbulence scale. Furthermore, since we measure the lateral water mass gradients along isopycnals, the signal is unaffected by the heave and vertical strain caused by internal waves.

4. Spectral Analysis Methods

The vertical profiles of temperature and salinity were processed as follows to compute horizontal wavenumber spectra of water mass anomalies along density surfaces. Profiles of T and S were vertically interpolated onto an evenly spaced density profile with 0.1 kg m^{-3} increments, effectively producing measurements of spice along isopycnal surfaces for each section. The longest section from each cruise is plotted in **Fig.6**, showing isopycnal spice anomalies. Since S , T and spice anomalies along isopycnals are proportional to one another, we need use only one to calculate statistics. We use S to be consistent with some of the previous literature (Kunze et al. 2015; Cole and Rudnick 2012). For each section that was approximately straight and longer than 100 km (all spice sections shown in **Fig. S2**), salinity anomalies along each isopycnal were horizontally linearly interpolated onto a regularly spaced distance grid with spacing smaller than the average profile spacing (2018: 100 m, 2015: 300 m, 2013: 3 km). Salinity along isopycnals $\sigma = 22$ and 25 are shown in **Fig.6**.

Spectra are calculated along each isopycnal using a Fast Fourier Transform (FFT) of detrended and Hanning-windowed segments. The Fourier coefficients are averaged over neighbouring isopycnals less than $\pm 0.5 \text{ kg m}^{-3}$ removed from the target isopycnals of $\sigma = 21, 22, \dots, 26$, and further

314 averaged in 10 logarithmically spaced wavenumber bins per decade (k in cycles per kilometer).
315 For clarity of presentation, and to facilitate the visual differentiation between negative slopes, the
316 plotted variance spectra $\mathcal{P}(k)$ are whitened by multiplying by $4\pi^2 k^2$, producing gradient spectra
317 $\mathcal{G}(k)$. These steps are shown in **Fig. S3**) for the $\sigma = 22$ and 25 isopycnals along the longest
318 section from 2015 shown earlier.

319 Following the procedure described in Appendix A of Klymak et al. (2015), we have also applied
320 a correction for variance lost at high wavenumbers due to finite sampling and horizontal gridding.
321 The correction was determined empirically by making synthetic spatial series of a k^{-2} (k^0) red-
322 noise process, applying exactly the same non-uniform sampling as the profile spacing from the
323 sections, interpolating onto a regular grid, and calculating spectral estimates as described above.
324 These estimates were then compared to spectra calculated from the full-resolution synthetic spatial
325 series. The roll-off is consistent with the empirical transfer function $\text{sinc}^2(\Delta x)$ with Δx equal to
326 the 0.67 times the mean separation between casts for each section. The correction is perhaps an
327 overestimate for the shallower isopycnals, since it assumes an underlying red-noise k^{-2} (k^0) signal,
328 whereas the observations at the fully resolved wavenumbers reveal an even steeper spectral fall-off
329 of k^{-3} (k^{-1}). Pseudo-code of the spectral analysis and roll-off correction method are provided in
330 the supplementary material.

331 For the 2013 large-scale survey cruise, with one section over 1000 km and three sections be-
332 tween 600 km and 700 km long, and an average UCTD profile spacing of 3 km, the spectral
333 estimate is confined between wavelengths of \sim 600 km and \sim 10 km. For the 2015 cruise with the
334 longest section over 400 km long, but the other sections between 100 km and 200 km long, and an
335 average FCTD profile spacing of 0.3 km, the spectral estimate is confined between wavelengths
336 of \sim 100 km and \sim 1 km. In contrast, during the 2018 cruise, the sections were sampled much
337 more slowly, with \sim 1 m s $^{-1}$ (2 kn) ship speeds, still at least double the speed of currents below

the ML, though of the same order of magnitude. Our sampling speed is ~ 3 times faster than the “slow” sampling tested in Rudnick and Cole (2011), which confirmed that spectral estimates from data collected along isopycnals with a slowly-moving platform, such as a glider, are reliable with regards to internal wave aliasing problems, but might be affected by a “Doppler smearing” of features in wavenumber space. Since thermohaline features in the ocean are not frozen, but move during the time it takes a ship to sample them, there is an uncertainty in the true distance between sampled horizontal features. Given the mean current and shear magnitudes relative to the ship speed, measured lengths of features of $O(1\text{-}10)$ km scales are estimated to differ from actual lengths at most by a factor of 2. This is treated as an uncertainty in wavenumber, but is relatively small given the logarithmic range of scales. Given the slower sampling, the spectral estimate from the 2018 data is confined between wavelengths of ~ 30 km and ~ 1 km. The spectral slopes from the 2018 data are generally consistent with the spectral slopes in the same wavenumber range from the 2015 data, which were sampled at faster ship speeds.

The individual spectra for each section, along each of the 6 isopycnal levels ($\sigma = 21$ to 26) are shown in **Fig.8**. While at some isopycnal levels ($\sigma = 23$ and 24) there is much variation between the spectra of individual sections (both between and within each of the 3 years), at isopycnal levels $\sigma = 22$ and 26 the spectra are consistent across all sections. At these isopycnal levels the spectra from the three separate cruises are consistent with each other at overlapping scales, even though the three hydrographic surveys sampled different seasons in different years. They cover a $1\sim 100$ km range of horizontal wavenumbers, with the 2013 data resolving long wavelengths (circa $10\sim 100$ km), the 2018 data resolving short wavelengths ($1\sim 10$ km), and the 2015 data resolving the entire range ($1\sim 100$ km). There are some differences in variance levels between the years, but the three datasets show the same general depth-dependent trends of decreasing variance levels and shallower spectral slopes with increasing depth. Given the large spread of spectral estimates

362 amongst the 14 sections plotted, we only show confidence bounds for the combined mean spectral
363 estimates calculated below.

364 For each tracer variance spectra corresponding to individual tracer sections in **Fig.8**, power law
365 slopes are estimated by a linear fit in log-log space over two scale ranges, from 10~100 km (2013
366 and 2015 data) and from 1~10 km (2015 and 2018 data). The individual slope estimates, the mean
367 for each scale range, and the standard deviations are shown in **Fig.9**. The uncertainty in slopes is
368 dominated by the spread between sections, and not by the much smaller uncertainty in estimating
369 the slope from each individual spectral estimate.

370 As an additional step, we calculate a mean spectral estimate for the entire BoB dataset along six
371 density surfaces, combining the individual spectra from 2013, 2015, and 2018. To combine the
372 individual spectra, they were first normalized by their variance levels at the wavenumber where
373 they overlap (0.1 cpkm), then wavenumber-bin averaged with a weight proportional to the length
374 of the corresponding sections, and then multiplied by the average of their variance levels at 0.1
375 cpkm. These spectral estimates reflect a variance weighted average, based on measurements made
376 along 14 sections that cumulatively span 4864 km of survey track, equivalent to ~50 independent
377 segments of 100 km length each. Given the spread in spectral slopes at some of the isopycnal
378 levels, if the individual spectra sampled different physical regimes, the slope of the mean spectra
379 are not necessarily an accurate representation of the true tracer distributions. This might be the
380 case especially for intermediate-depth isopycnal levels ($\sigma = 23$ and 24), however the individual
381 spectral slopes at shallower and deeper isopycnal levels ($\sigma = 22$ and 26), at scales of 1~10 km,
382 are much more consistent with each other.

383 For these combined spectral estimates (**Fig.10**), estimates of 90% confidence bounds are calcu-
384 lated with a chi-squared distribution following Klymak et al. (2015). Degrees of freedom are equal
385 to the number of independent spectral estimates within each wavenumber bin. This is estimated

as twice the number of squared Fourier coefficients that are averaged (by averaging over different segments and over adjacent wavenumber bands) to form the estimate within each wavenumber band, reduced by an ad-hoc factor (3) to be conservative. The sum accounts for coefficients from FFT's for all (9) isopycnal layers near each target isopycnal, but reduces this by an ad-hoc factor (linearly increasing from 2 at the highest wavenumbers to 4 at the lowest wavenumbers) to account for the vertical correlation of anomalies between neighbouring isopycnal layers. The wavenumber-dependence of the factor is chosen in approximation of the results of Klymak et al. (2015), who found a scale-dependent vertical correlation. A visual inspection of salinity anomalies along neighbouring isopycnals (**Fig. S3**) supports this approach, as large-scale anomalies seem more correlated than small-scale anomalies between nearby isopycnals. Furthermore, the signals of interest in the spectra, such as clear changes of slope, are much larger than the uncertainty estimate.

5. Results: Tracer Spectra

The tracer spectra from the three expeditions offer a robust estimate of the variance distribution ranging from $O(100)$ – $O(1)$ km in the upper pycnocline of the BoB. Both the variance levels and the spectral slopes of variance distributions are depth-dependent, with generally deeper isopycnals containing less variance and less red spectral variance slopes compared to shallower isopycnals. The salinity variance along isopycnals shallower than 100 m is most strongly elevated at scales of 10–100 km, where the variance is 2 orders of magnitude greater than the variance along the deepest isopycnal at about 180 m.

However, on the shallower isopycnals (< 100 m), the elevated variance falls off steeply below 10 km scales, with spectra along the $\sigma = 22$ isopycnals exhibiting power laws $\mathcal{P}(k) \sim k^{-2.9 \pm 0.2}$ ($\mathcal{G}(k) \sim k^{-0.9 \pm 0.2}$) (**Fig.9**). The $O(10)$ km scale at which this change in spectral slope occurs

409 coincides with the local Rossby radius of deformation in the surface mixed layer NH_{ML}/f (Callies
410 et al. 2016), where we estimate $N \sim 0.01 \text{ s}^{-1}$ and $H_{ML} \sim 30\text{--}50 \text{ m}$ from the mean stratification
411 profiles in **Fig.5**. Coriolis frequency f ranges from 1×10^{-5} to $5 \times 10^{-5} \text{ s}^{-1}$ depending on the
412 latitude of the cruise track.

413 The steepening of the spectrum at scales smaller than circa 10 km (scales resolved in 2015
414 and 2018) is seen consistently along the $\sigma = 22$ isopycnals, as well as along the $\sigma = 21$ and
415 23 isopycnals for many sections, and along the $\sigma = 24$ isopycnal along a few sections (**Fig.8**).
416 During the 2015 cruise the $\sigma = 21$ and 22 isopycnals occasionally outcropped into the ML or
417 into the weakly stratified layers in between the peak stratification depth and the ML base, yet the
418 spectral steepening is also present along isopycnals that always remained at depths below the peak
419 stratification, such as the $\sigma = 22$ isopycnal in 2018 and the $\sigma = 23$ isopycnal in 2015 (**Fig.5**).

420 Salinity variance is in general highest along the shallowest isopycnal that is located within or
421 just below the peak stratification. Salinity variance is reduced in some of the sections along the
422 shallowest isopycnal ($\sigma = 21$), when it is located in weakly stratified layers above the peak strat-
423 ification, such as during some of the 2013 and 2015 sections. This indicates that these weakly
424 stratified layers are remnant mixed layers containing signatures of surface boundary forcing and
425 variance dissipation.

426 A qualitative assessment by eye of the salinity anomaly or salinity variance on isopycnals (**Fig.6**
427 or **Fig.7**) is consistent with the spectra that are calculated. For example, the salinity along the
428 shallower isopycnals in the 100 km long transects of the 2018 data has smaller-scale fluctuations
429 of lesser magnitude than the large-scale variability seen in the longer sections from 2013 (i.e. a
430 red gradient spectrum). Lastly, to complement the spectral analysis, the isopycnal salinity mea-
431 surements were also analyzed using a wavelet decomposition. The results again show the same

432 scale-dependence of variance, with a lack of variance at 1–10 km scales relative to 10–100 km
433 scales along the shallower isopycnals (supplementary **Fig. S4**).

434 6. Discussion

435 The observations of T , S or spice variability analysed in this study along isopycnals, are in some
436 cases, associated with thermohaline intrusions or inversions in T or S (Ruddick and Kerr 2003).
437 In Jaeger et al. (2019) we analyse the layers in spice that cross isopycnal surfaces and explain
438 their formation. Our analysis suggests that double diffusion does not play a significant role in the
439 formation of these layers, but frontal instabilities can generate intrusions or layering Woods and
440 Fischer (1986). Other types of dynamical instabilities could also create different sorts of lateral
441 stirring environments at various depths, as described in Hua et al. (2013).

442 This study presents a robust set of passive tracer spectra from the relatively sparsely sampled
443 Indian Ocean (**Fig.11**), finding depth-dependent and scale-dependent spectral slopes that are in
444 part inconsistent with current theories of tracer stirring by ocean currents. We compare our results
445 with the few other published studies of tracer spectra in the world oceans and discuss differences
446 in environments and the potential role of submesoscale ocean dynamics that could explain the
447 differences in the tracer spectra.

448 a. *Contextualizing the Bay of Bengal Study*

449 There have been several studies in the Pacific and two in the Atlantic Ocean of the statistics of
450 spatial distributions of spice, or compensated salinity or temperature anomalies along an isopyc-
451 nyal. We briefly summarize them here, and compare linear fits of their spectral slopes with our
452 observations in **Fig.10**.

453 Analysis of observations from the towed instruments in the ‘Spice’ expedition (Callies and Fer-
454 rari 2013) and from repeated glider sections (Cole and Rudnick 2012) in the subtropical North
455 Pacific at depths between 100 and 800 m, consistently found isopycnal tracer spectra with k^{-2}
456 (k^0) behavior at \sim 10–100 km scale wavelengths (**Fig. 10**). This depth-independent power law
457 is inconsistent with both interior QG theory that predicts spectra to follow k^{-1} (k^{+1}), as well as
458 surface-QG modes that would predict steeper spectra below the surface.

459 Another recent analysis (Klymak et al. 2015) of profiler observations in the Gulf of Alaska (‘Line
460 P’) and undulating towed measurements in the subtropical Northern Pacific (‘IWAP’) also found
461 tracer spectra between 10–100 km scales to be inconsistent with QG/SQG theory. They instead
462 found power laws usually between $k^{-1.5}$ ($k^{0.5}$) and $k^{-1.7}$ ($k^{0.3}$), and reddening towards k^{-2} (k^0)
463 along the deepest isopycnals at around 150 m along Line P. While finding less red spectra than
464 the previous studies, the observed reddening with depth trend is exactly opposite to the expected
465 decay of SGQ modes and increasing dominance of interior-QG modes with increasing depth.

466 A wavelet analysis of glider data (‘CUGN’) from the upper 500 m of the California Current
467 System, resolving spectra over the narrow wavelength range of 12–60 km, found a change in slope
468 with scale in their isopycnal salinity gradient spectra (Itoh and Rudnick 2017). On average, across
469 the seasons and inshore/offshore regions, they estimate a k^{-1} (k^{+1}) slope in their “mesoscale”
470 lower half range, and a k^{-2} (k^0) slope in their “submesoscale” upper half range. They interpret
471 the flat part of the spectrum, at scales smaller than the baroclinic Rossby radius, as the signature
472 of sharp fronts.

473 A recent study (McCaffrey et al. 2015) applied a novel technique to the global Argo profile
474 dataset, calculating salinity structure functions from scattered profiles instead of spectra along
475 transects. They found equivalent isopycnal tracer spectra power laws of $k^{-1.7}$ ($k^{0.3}$) between
476 10–100 km scales, but with little dependence on depth in the upper 2000 m. Their results are

⁴⁷⁷ broadly consistent with the other mesoscale studies. The same structure function technique was
⁴⁷⁸ also applied to a glider dataset from the open ocean in the northeast Atlantic ('OSMOSIS') Er-
⁴⁷⁹ ickson et al. (2020). They found little vertical variation in structure function slopes of passive
⁴⁸⁰ tracers, with slopes equivalent to spectra power laws of $k^{-1.5}$ ($k^{0.5}$). However their results suggest
⁴⁸¹ significant transfer of submesoscale variability between the surface ML and the interior occurs
⁴⁸² throughout the year, raising the importance of motions that stir at submeso-scales in the interior.

⁴⁸³ In the subtropical Atlantic Ocean, the 'NATRE' study (Ferrari and Polzin 2005) calculated struc-
⁴⁸⁴ ture functions from *TS* observations between 900 and 1200 m depth, finding equivalent isopycnal
⁴⁸⁵ tracer spectra power laws of $k^{-1.2}$ ($k^{0.8}$) between 2–100 km scales. Extending to smaller scales,
⁴⁸⁶ the 'LatMix' study (Kunze et al. 2015) in the North Atlantic's Sargasso Sea found tracer spectral
⁴⁸⁷ slopes again approximately equal to k^{-2} (k^0) over wavelengths ranging from 10 km to 0.03 km in
⁴⁸⁸ the seasonal pycnocline between 20–60 m depth. However, measurements along a larger survey
⁴⁸⁹ track (referred to as the MVP and Triaxus surveys) that resolved wavelengths between 10 and
⁴⁹⁰ 1 km, found very red spectra estimated to lie between k^{-3} (k^{-1}) and $k^{-2.5}$ ($k^{-0.5}$) in the 5 to
⁴⁹¹ 1.4 km wavelength band. Spanning less than a decade of wavenumbers, this estimate was deemed
⁴⁹² less robust than the main results of the study.

⁴⁹³ In summary, five of the six published studies found tracer gradient spectra with power laws close
⁴⁹⁴ to k^{-2} (k^0), inconsistent with QG predictions, but consistent with ageostrophic frontogenesis the-
⁴⁹⁵ ory. The power law slopes were generally also independent of depth, or in some cases became
⁴⁹⁶ less red towards shallower depths, in contrast to the SQG or surface-frontogenesis predictions of
⁴⁹⁷ redder slopes near the surface. An exception is reported, albeit without stating a degree of con-
⁴⁹⁸ fidence, in the LatMix dataset, which found a red gradient spectral slope between 5 and 1.4 km
⁴⁹⁹ wavelengths, with the same k^{-3} (k^{-1}) power law that we report along shallow isopycnals in the
⁵⁰⁰ BoB. Perhaps it is notable that both the BoB and the LatMix studies are in regions with elevated

frontogenetic potential at the surface due to an energetic mesoscale, compared to the studies from the subtropical and northern Pacific. The BoB has a seasonal western boundary current that stands out in the climatological eddy kinetic energy (EKE) map (**Fig.11**), with elevated EKE in the central BoB as well. The present study is also at lower latitudes (5–18°N) than all the above cited studies of along-isopycnal tracer spectra (all located between 23–50°N). The present region's smaller Coriolis parameter leads to longer inertial periods and larger deformation scales.

One potential reason that the reddening of the spectral slopes reported here was not seen in previous studies could be that this is one of the few (if only) studies that measured lateral variations in temperature and salinity in the stratified region below the surface mixed layer at such fine horizontal resolution, and over such long distances and short time periods. The combination of vertical and horizontal resolution over vast distances helped to generate robust statistics. Furthermore, the large-scale contrast in spice along isopycnals provides a source for the spice variance in the BoB. The intense density stratification inhibits vertical mixing and preserves the signals of horizontal stirring. The possibility remains that the Bay of Bengal has unique mixing characteristics, at least compared to the oceanic settings of previous observations of spice distributions.

b. Interpreting Bay of Bengal Spectra

The classical interpretation of wavenumber spectra of a passive tracer in the ocean interior assumes an injection (source) of tracer variance at large scales (small wavenumbers), a downscale cascade, and a sink of variance at small scales (large wavenumbers). If the statistics averaged over a large enough region are stationary, the variance level at any particular scale in between the forcing and the dissipative scales, depends on how efficiently gradients are strained into smaller features by the 2-dimensional turbulence, and the dissipation rate of tracer variance through 3-dimensional turbulent mixing. Tracer gradients in the interior can also retain signals from external

forcing such as air-sea fluxes acting on the surface ML that are then re-stratified and entrained into the interior. Destruction of variance only occurs at the scale of 3-dimensional isotropic turbulent mixing, which can act only on gradients at that scale. Within this framework, the slopes of isopycnal salinity spectra in the upper 200 m of the BoB at scales between 1–100 km tell a depth-dependent story with three parts.

First, at depths of 150–200 m ($\sigma = 26$), the tracer variance level decays with increasing wavenumber following an approximately $k^{-1.7 \pm 0.3}$ ($k^{0.3 \pm 0.3}$) power law (**Fig.8F and Fig.9F**). This is in agreement with theories of stratified turbulence, which predict tracer variance distributions follow the Obukhov-Corrsin spectrum $\mathcal{P}(k) = C \cdot \chi \cdot \varepsilon^{-1/3} \cdot k^{-5/3}$, where χ is the turbulent temperature flux rate or dissipation rate, ε the turbulent energy dissipation rate, and $C \approx 0.5$ is an empirical constant (Brethouwer and Lindborg 2008). Fitting the theoretical spectrum to observed variance levels, and assuming ε is between 10^{-10} and $10^{-8} \text{ W kg}^{-1}$, the temperature variance flux rate χ is predicted to be between 10^{-10} and $10^{-9} \text{ W kg}^{-1}$. The observed spectral slope is also in agreement with predictions for tracer spectra stirred by two-dimensional geostrophic turbulence in an inverse energy cascade range above the stirring scale (Vallis 2017). However, it is unlikely that the dominant stirring at these depths is by motions or eddies of $O(1)$ km or smaller; instead the deeper currents are due to the mesoscale eddy field. The slope is also in agreement with SQG predictions, which would necessitate surface modes to penetrate 150–200 m to the $\sigma = 26$ isopycnal layer, even though this depth is clearly below the peak pycnocline and insulated from surface boundary forcing. Estimating the penetration depth H by $\frac{f}{N} \cdot L \sim \frac{3 \cdot 10^{-3}}{0.02} \cdot L$, 10 km wide eddies would penetrate only 20 m, while 100 km eddies do reach 200 m.

Next, at shallow depths of around 40 to 70 m ($\sigma = 22$), the spectra also show an approximately $k^{-1.7 \pm 0.6}$ ($k^{0.3 \pm 0.6}$) power law above $O(10)$ km scales, but an unexpected finding is that they consistently steepen to $k^{-2.9 \pm 0.2}$ ($k^{-0.9 \pm 0.2}$) at scales smaller than $O(10)$ km (**Fig.8B and Fig.9B**).

548 The σ 22 isopycnal surface is found both within and just beneath the depth of strongest stratification (Fig.5). This change in slope at $O(10)$ km scales suggests a change in dominant dynamics
549 around the ML Rossby deformation radius ($\sim NH_{ML}/f$).
550

551 Finally, at intermediate depths of around 60 to 150 m (σ 23–25), tracer variance spectra do
552 not have a consistent slope between all 14 sections, but instead show a range of power slopes in
553 between k^{-1} and k^{-3} (gradient spectral slopes between k^{+1} and k^{-1}) (Fig.8C-E and Fig.9C-E).
554 Some spectra at σ 23 and 24, isopycnals located always within the pycnocline, show similarly
555 steep slopes as the spectra at σ 22. Spectral analysis does not identify what process is responsible
556 for the steeper fall-off in tracer variance at scales below $O(10)$ km and at stratified depths of up to
557 100 m, or 3 to 4 times the ML depth.

558 The average of all spectra below $O(10)$ km scales has a power law slope of approximately $k^{-2.0}$
559 ($k^{0.0}$), inconsistent with interior QG, somewhat less inconsistent with SQG or stratified turbulence
560 predictions under idealised conditions, but consistent with other observational studies. It poten-
561 tially indicates that mesoscale frontogenesis and ageostrophic dynamics cascade variance more
562 rapidly than predicted by QG dynamics in the pycnocline (Klein et al. 1998). The on average
563 redder slopes at these intermediate depths relative to the deeper ($\sigma = 26$) average spectrum is
564 consistent with the notion that more small-scale stirring and straining increases the rate of down-
565 scale variance flux more at smaller scales along the tracer cascade, steepening the spectrum, and
566 that ageostrophic small-scale motions attenuate over a shallower depth than geostrophic mesoscale
567 currents.

568 However, the average of these spectra is not necessarily an appropriate measure if two distinct
569 physical regimes are leading to two distinct tracer variance distributions, forming an approxi-
570 mately k^{-3} power law spectrum at depths above about 70 m, and an approximately k^{-1} spectrum
571 below 150 m depths. While the literature regularly compares spectral observations with theory,

the agreement or disagreement of tracer spectral slopes with theoretical predictions should be interpreted carefully. Predictions are made using idealized assumptions, such as homogeneity and scale-separation, which allows an inertial range to form. These idealized conditions are unlikely to adequately represent the real conditions in the BoB, where for example kinetic energy might be input at various scales by ML instabilities and atmospheric forcing. More significant than observations of particular slopes are changes in spectral slopes, at particular scales, or between particular depths, indicating a change in the dynamics of the variance cascade. The observed steepening of the tracer variance spectra around scales of 10 km indicates a change in the rate-limiting process that transfers variance downscale.

581 c. Potential Explanations

582 Might the unusual spectral slope of tracer variance observed along the shallower isopycnals simply be the signature of water mass anomalies subducted or injected into the interior from the surface ML? This explanation by itself seems unlikely, since we observe not an excess, but a lack, of variance at smaller scales. Such reduced levels of variance at relatively smaller $O(1)$ km scales should be temporary, given the relative excess of variance present at larger $O(10 - 100)$ km scales that could be cascaded down-scale. We expect a downscale tracer variance cascade, whether described by QG or ageostrophic theory, to transfer variance across scales (from large to smaller spatial scales), within the timescale of the background mesoscale stirring and straining, which is of $O(10)$ days, given the mean EKE in the BoB of $O(0.1) \text{ m}^2 \text{ s}^{-2}$ and mesoscale eddies of $O(100)$ km scale. Yet low oxygen levels (**Fig.2B**) at the $\sigma = 23$ isopycnal, which never outcropped in the BoB observations, suggest that water mass anomalies within this layer have residence timescales below the surface ML considerably longer than the timescale of stirring. Thus, if the deficit of 1-km-scale tracer variance along the $\sigma = 23$ isopycnal is a remnant signature of mixing in the surface ML prior

595 to watermass subduction, the small-scale variance should be replenished by a downscale variance
596 cascade in the time since the water layer was last ventilated. The fact that small-scale variance is
597 ‘missing’, in layers that have been insulated from surface-forced mixing for a relatively long time,
598 calls for a different explanation.

599 We are left with two categories of potential explanations, schematically represented in **Fig.12**,
600 and further discussed below. The observed steepening of tracer spectra below 10 km is either
601 caused by (mixing) processes actively decreasing variance at scales below 10 km, or by a suppres-
602 sion in the downscale spectral flux of variance below 10 km scales.

603 1) ENHANCED HORIZONTAL MIXING AT SCALES BELOW 10 KM

604 We propose two candidates for adding effective mixing, which are not mutually exclusive, and
605 could enhance tracer variance diffusion within the pycnocline and explain the steep decay of vari-
606 ance below $O(10)$ km. One is submesoscale frontal instabilities and associated submesoscale
607 circulations that penetrate below the ML (input of energy, not necessarily watermass, into the
608 stratified interior), while another is shear dispersion powered by near-inertial generated waves
609 (NIW) with very small vertical wavelengths in the strongly stratified pycnocline. Both expla-
610 nations would need to produce spice patterns with large aspect ratios (long and thin), such that
611 turbulent vertical mixing effectively removes variance at submesoscales (Smith and Ferrari 2009).

612 Submesoscale instabilities convert the potential energy of lateral buoyancy gradients (usually but
613 not exclusively in the ML) into kinetic energy, and through interactions with the mesoscale strain
614 field, can transfer energy from the mesoscale to submeso- and dissipative scales (McWilliams
615 2016). The surface ML of the BoB is characterized by strong density fronts with buoyancy gra-
616 dients at least one order of magnitude stronger at scales of $O(1)$ km compared to the mesoscale
617 buoyancy gradients at scales $O(10\text{--}100)$ km (**Fig.13**). This ratio is calculated by comparing the

618 largest magnitudes (1 and 0.1 percentile) of density gradients in spatial transects smoothed by
619 low-pass filters (3rd order Butterworth) with cutoff wavenumbers ranging from equivalent wave-
620 lengths of 0.5 to 50 km. Signatures of submesoscale frontal processes at $O(1\text{--}10)$ km scales have
621 been observed in the BoB (Ramachandran et al. 2018). ML eddies generated from baroclinic
622 instabilities can also penetrate below the ML into the pycnocline, stirring water masses along
623 isopycnals (Badin et al. 2011) and enhancing the effective lateral diffusivity at submesoscales.

624 The observed tracer variance fall-off below 10 km scales along isopycnals that lie just be-
625 neath the ML, could be caused by enhanced stirring by submesoscale instabilities that are ac-
626 tive within the mixed layer, powered by strong freshwater-controlled potential energy gradients
627 or other sources of flow instabilities. The extra submesoscale stirring needs to act only at scales
628 smaller than $O(10)$ km, reducing variance in the $O(1)$ km band. The energy input by such subme-
629 soscale instabilities would invalidate the assumption of an inertial range by the theoretical slope
630 predictions, and complicate interpretations of spectral slopes as related to rates of variance transfer.

631 The spectral fall-off could potentially also be due to shear dispersion enhancing effective along-
632 isopycnal diffusivity. Internal-wave shear dispersion allows weak turbulent mixing at small scales
633 to effectively diffuse lateral gradients at larger scales much more quickly than expected (Young
634 et al. 1982). A sheared flow, whether or not reversible, tilts tracer isopleths to enhance the cross-
635 diapycnal area of a water mass anomaly compared to its lateral (along-isopycnal) dimension, and
636 amplify the weak but widespread vertical diffusion K_v into a much greater lateral diffusion $K_h \sim$
637 $(V_z/f)^2 K_v$, where V_z is the average vertical shear magnitude (Shcherbina et al. 2015).

638 Observations in the BoB reveal strongly sheared upper ocean currents dominated by shear layers
639 of $O(10)$ m thickness, with an average vertical shear of magnitude 0.01 s^{-1} (Lucas et al. 2016;
640 Shroyer et al. 2019). Given the small average Coriolis parameter in the BoB of $f = 3 \times 10^{-5} \text{ s}^{-1}$,
641 the effective isopycnal diffusivity is enhanced by a factor of 10^5 over the diapycnal diffusivity.

However, observations in the BoB show weak turbulence below the ML, with median values of the diapycnal diffusivity $K_v = 10^{-6} \text{ m}^2 \text{ s}^{-1}$ in the pycnocline, interspersed with sporadic elevated values of up to $10^{-3} \text{ m}^2 \text{ s}^{-1}$ in the upper 50 m (Shroyer et al. 2016; Lucas et al. 2016). Thus the average effective lateral diffusivity is estimated to be $O(0.1) \text{ m}^2 \text{ s}^{-1}$ below 50 m depth, similar to other estimates, yet an order of magnitude smaller than what was estimated from dye-release experiments in the coastal ocean south of Martha's Vineyard (Sundermeyer and Ledwell 2001) and in the Sargasso Sea (Shcherbina et al. 2015). However, within the top of the shallow pycnocline, right below the ML, vertical diffusivities of $K_v = 10^{-5} \text{ m}^2 \text{ s}^{-1}$ do not seem unreasonable, and thus lateral diffusivities K_h could be enhanced to values of $O(1) \text{ m}^2 \text{ s}^{-1}$. In addition, if enhanced vertical shear is correlated with intermittent enhanced turbulent mixing (Kunze and Sundermeyer 2015), effective lateral mixing could intermittently be an order of magnitude larger.

If shear dispersion in the BoB is driven by near inertial waves, which generate oscillatory shear, the spatial scales over which the effective diffusivity acts is equal to the spatial scales of the oscillation's lateral excursions. This scale is estimated as $\Delta z \cdot V_z \cdot \frac{1}{f}$, where Δz is the vertical scale of the oscillation. Given a shear of 0.01 s^{-1} across 10 m thick layers, the horizontal scale is $O(1) \text{ km}$. It is thus plausible that on the shallowest isopycnal surfaces in the top 100 m of the BoB, shear dispersion, acting on lateral gradients of $O(1) \text{ km}$ scales, enhances isopycnal diffusivity to $O(1 - 10) \text{ m}^2 \text{ s}^{-1}$. This would effectively reduce tracer variance at submesoscales, and potentially lead to the steep spectral fall-off, perhaps aided by the low-latitude and high-stratification of the BoB that favor strong NIW shear layers with very thin vertical extent.

2) INHIBITED CASCADE OF COHERENT WATER MASS ANOMALIES

A reduction in the downscale cascade of tracer variance from larger scales could also explain the steepened spectral slope of spice variance below 10 km scales. One way for this to occur is if the

tracer distribution is correlated to the flow field in a manner that the eddy stirring and straining is ineffective at breaking apart the tracer's 10–100 km scale patterns. For example, the tracer distribution could be modulated by coherent structures in the flow, or correlated with potential vorticity (PV) anomalies formed by past subduction or entrainment of water masses from the surface or frictional bottom (lateral) boundary layers. In such a case, the assumption that macro-turbulence is stochastic and homogeneous is invalid. Both in 2013 and 2015, we encountered mesoscale eddies with an anomalous fresh-cold water mass visible in the core **Fig.S2**, and reported in (Gordon et al. 2017), while on a smaller scale, submesoscale subduction was seen to create anomalous stratification and water mass anomalies at fronts (Ramachandran et al. 2018). Another possible mechanism correlating water mass anomalies with PV is capping. If the spice contrast across a compensated TS front is large enough, isopycnal mixing leads to an increase in density, generating small-scale vertical mixing Thomas and Shakespeare (2015). Occurring within strong stratification, this process would create thin, well-mixed, low-PV regions with distinct TS characteristics. Further investigation into the viability of this potential PV-spice coherence creation mechanism is needed.

If the observed steep spectral slope is indeed due to an inhibited spice variance cascade, then water mass distributions in the BoB are not a measure of a random passive tracer being isopycnally stirred, but rather a tracer that, though strictly passive, is correlated with dynamical properties and coherent flow structures. However, even if currents are partially correlated with water mass anomalies, the propagating mesoscale eddy flow field would still be expected to encounter uncorrelated tracer gradients of $O(100)$ km scales, and strain these to $O(1–10)$ km scales, thereby replenishing the “missing” variance levels along isopycnals in the interior.

687 **7. Concluding Remarks**

688 We present a synthesis of along-isopycnal spice variance measured from 3 cruises in the Bay
689 of Bengal and find that along isopycnals in the strongly stratified upper 75 m, the tracer vari-
690 ance spectra are much more steeply sloping ($\mathcal{P}(k) \sim k^{-3}$) in the submesoscale regime than can
691 be explained by existing theories of 2-dimensional macro-turbulence. The lack of spice variance
692 at 1–10 km scales relative to the variance levels at 10–100 km scales means that the horizontal
693 gradients between warm-salty and cold-fresh features are too smooth between 1–10 km scales to
694 be consistent with QG or frontogenetic dynamics. This indicates that in this regime, either hori-
695 zontal mixing is more effective than expected, or water mass anomalies are less effectively stirred
696 and strained into 1 km scale features. The first, more likely, explanation invokes the importance
697 of submesoscale processes for horizontal mixing, whether they be vortical or wavelike in nature.
698 Enhanced shear dispersion by NIWs with very small vertical wavelengths are a promising candi-
699 date. The latter explanation would mean that spice spectral distributions do not reflect stirring by
700 homogeneous macro-turbulence of an independent, stochastically distributed tracer, but rather the
701 distribution of a dynamically relevant property.

702 At depths between 100 and 200 m, the flattening of spectra suggests that tracer stirring dom-
703 inated by frontogenesis ($\mathcal{P}(k) \sim k^{-2}$) transitions towards stirring driven by stratified turbulence
704 or SQG dynamics ($\mathcal{P}(k) \sim k^{-5/3}$) with depth. These findings differ from similar observational
705 studies in the Atlantic and Pacific Oceans, which did not observe the steep tracer spectra in the
706 submesoscale range, nor the significant flattening of spectra with increasing isopycnal depth. The
707 results attest to the strong stratification and separation between processes stirring the upper 40–
708 70 m of the pycnocline, the intermediate layers around 100 m, and the more quiescent interior
709 around 200 m.

710 The results from this study demonstrate that 2-dimensional macro-turbulence in the ocean is not
711 yet completely understood. The lack of 1-km scale variance calls attention to the potential role
712 of submesoscale dynamics and near-inertial waves, or their interactions, in controlling horizontal
713 mixing in the upper ocean, and to potential misinterpretations of spice anomalies. A proper ac-
714 counting of submesoscale and wave-like oscillatory processes is important for the development of
715 model sub-grid parameterizations.

716 *Acknowledgments.* We are grateful to the captain and crew of the R/V Roger Revelle and the R/V
717 Thomas G. Thompson, and all ASIRI-OMM and MISO-BOB scientists. This work was carried
718 out under the Office of Naval Research’s “Air-Sea Interaction Regional Initiative – ASIRI” and
719 “Monsoon Intra-Seasonal Oscillations in the Bay of Bengal – MISO-BOB” research initiatives, in
720 collaboration with the Indian Ministry of Earth Science’s “Ocean Mixing and Monsoons” (OMM)
721 initiative supported by the “Monsoon Mission”. Support came from ONR grants N00014-16-1-
722 2470, N00014-13-1-0451, N00014-17-1-2390 (G.S.J. and A.M.), N00014-14-1-0455 (J.M. and
723 J.N), N00014-17-1-2511 (J.M.), N00014-13-1-0489, N00014-17-1-2391 (A.L.), N00014-15-1-
724 2634 (E.S.), N00014-13-1-0456, N00014-17-1-2355 (A.T.), and N00014-13-1-0453, N00014-17-
725 1-2880 (J.F.).

726 All authors declare that they have no competing interests. All data needed to evaluate the con-
727 clusions in the paper are present in the paper and/or the Supplementary Materials. Additional data
728 related to this paper may be requested from the authors.

729 Used in Fig.2, SMAP salinity data are produced by Remote Sensing Systems and sponsored
730 by the NASA Ocean Salinity Science Team. Data are available at www.remss.com. Used in Fig.
731 3, the altimeter products were produced and distributed by Aviso+ (www.aviso.altimetry.fr), as
732 part of the Ssalto ground processing segment. Used in Fig.11, the Ssalto/Duacs altimeter products

⁷³³ were produced and distributed by the Copernicus Marine and Environment Monitoring Service
⁷³⁴ (CMEMS) (www.marine.copernicus.eu).

735 **References**

- 736 Badin, G., A. Tandon, and A. Mahadevan, 2011: Lateral mixing in the pycnocline by baroclinic
737 mixed layer eddies. *Journal of Physical Oceanography*, **41** (11), 2080–2101.
- 738 Brethouwer, G., and E. Lindborg, 2008: Passive scalars in stratified turbulence. *Geophysical Re-*
739 *search Letters*, **35** (6).
- 740 Callies, J., and R. Ferrari, 2013: Interpreting energy and tracer spectra of upper-ocean turbulence
741 in the submesoscale range (1–200 km). *Journal of Physical Oceanography*, **43** (11), 2456–2474.
- 742 Callies, J., G. Flierl, R. Ferrari, and B. Fox-Kemper, 2016: The role of mixed-layer instabilities in
743 submesoscale turbulence. *Journal of Fluid Mechanics*, **788**, 5–41.
- 744 Capet, X., J. C. McWilliams, M. J. Molemaker, and A. Shchepetkin, 2008: Mesoscale to subme-
745 soscale transition in the California current system. part iii: Energy balance and flux. *Journal of*
746 *Physical Oceanography*, **38** (10), 2256–2269.
- 747 Cole, S. T., and D. L. Rudnick, 2012: The spatial distribution and annual cycle of upper ocean
748 thermohaline structure. *Journal of Geophysical Research: Oceans*, **117** (C2).
- 749 D’Asaro, E. A., and Coauthors, 2018: Ocean convergence and the dispersion of flotsam. *Proceed-
750 ings of the National Academy of Sciences*, 201718453.
- 751 Erickson, Z. K., A. F. Thompson, J. Callies, X. Yu, A. N. Garabato, and P. Klein, 2020: The
752 vertical structure of open-ocean submesoscale variability during a full seasonal cycle. *Journal*
753 *of Physical Oceanography*, **50** (1), 145–160.
- 754 Essink, S., V. Hormann, L. R. Centurioni, and A. Mahadevan, 2019: Can we detect submesoscale
755 motions in drifter pair dispersion? *Journal of Physical Oceanography*, **49** (9), 2237–2254.

- 756 Ferrari, R., and K. L. Polzin, 2005: Finescale structure of the t-s relation in the eastern north
757 atlantic. *Journal of Physical Oceanography*, **35** (8), 1437–1454.
- 758 Gordon, A. L., E. Shroyer, and V. Murty, 2017: An intrathermocline eddy and a tropical cyclone
759 in the Bay of Bengal. *Scientific Reports*, **7**, 46 218.
- 760 Gordon, A. L., E. L. Shroyer, A. Mahadevan, D. Sengupta, and M. Freilich, 2016: Bay of bengal:
761 2013 northeast monsoon upper-ocean circulation. *Oceanography*, **29** (2), 82–91.
- 762 Hua, B. L., C. Ménesguen, S. Le Gentil, R. Schopp, B. Marsset, and H. Aiki, 2013: Layer-
763 ing and turbulence surrounding an anticyclonic oceanic vortex: in situ observations and quasi-
764 geostrophic numerical simulations. *Journal of Fluid Mechanics*, **731**, 418–442.
- 765 Itoh, S., and D. L. Rudnick, 2017: Fine-scale variability of isopycnal salinity in the california
766 current system. *Journal of Geophysical Research: Oceans*, **122** (9), 7066–7081.
- 767 Jaeger, G. S., A. J. Lucas, and A. Mahadevan, 2019: Formation of interleaving layers in the bay
768 of bengal. *Deep Sea Research Part II: Topical Studies in Oceanography*, 104717.
- 769 Jaeger, G. S., and A. Mahadevan, 2018: Submesoscale-selective compensation of fronts in a
770 salinity-stratified ocean. *Science Advances*, **4** (2), e1701 504.
- 771 Jaeger, S. G. V. R., 2019: Stratified and stirred: Monsoon freshwater in the Bay of Bengal. Ph.D.
772 thesis, Massachusetts Institute of Technology.
- 773 Jinadasa, S., I. Lozovatsky, J. Planella-Morató, J. D. Nash, J. A. MacKinnon, A. J. Lucas, H. W.
774 Wijesekera, and H. J. Fernando, 2016: Ocean turbulence and mixing around Sri Lanka and in
775 adjacent waters of the northern Bay of Bengal. *Oceanography*, **29** (2), 170–179.
- 776 Klein, P., A.-M. Treguier, and B. L. Hua, 1998: Three-dimensional stirring of thermohaline fronts.
777 *Journal of Marine Research*, **56** (3), 589–612.

- 778 Klymak, J. M., W. Crawford, M. H. Alford, J. A. MacKinnon, and R. Pinkel, 2015: Along-
779 isopycnal variability of spice in the north pacific. *Journal of Geophysical Research: Oceans*,
780 **120** (3), 2287–2307.
- 781 Kunze, E., J. Klymak, R.-C. Lien, R. Ferrari, C. Lee, M. Sundermeyer, and L. Goodman, 2015:
782 Submesoscale water-mass spectra in the sargasso sea. *Journal of Physical Oceanography*,
783 **45** (5), 1325–1338.
- 784 Kunze, E., and M. A. Sundermeyer, 2015: The role of intermittency in internal-wave shear disper-
785 sion. *Journal of Physical Oceanography*, **45** (12), 2979–2990.
- 786 Lapeyre, G., and P. Klein, 2006: Dynamics of the upper oceanic layers in terms of surface quasi-
787 geostrophy theory. *Journal of Physical Oceanography*, **36** (2), 165–176.
- 788 Lévy, M., R. Ferrari, P. J. Franks, A. P. Martin, and P. Rivière, 2012: Bringing physics to life at
789 the submesoscale. *Geophysical Research Letters*, **39** (14).
- 790 Lucas, A. J., and Coauthors, 2016: Adrift upon a salinity-stratified sea: A view of upper-ocean
791 processes in the bay of bengal during the southwest monsoon. *Oceanography*, **29** (2), 134–145.
- 792 MacKinnon, J., L. St Laurent, and A. C. N. Garabato, 2013: Chapter 7 - diapycnal mixing pro-
793 cesses in the ocean interior. *Ocean Circulation and Climate*, International Geophysics, Vol. 103,
794 Academic Press, 159–183.
- 795 McCaffrey, K., B. Fox-Kemper, and G. Forget, 2015: Estimates of ocean macroturbulence: Struc-
796 ture function and spectral slope from argo profiling floats. *Journal of Physical Oceanography*,
797 **45** (7), 1773–1793.
- 798 McWilliams, J. C., 2016: Submesoscale currents in the ocean. *Proc. R. Soc. A*, **472** (2189),
799 20160117.

- 800 Meissner, T., F. Wentz, and A. Manaster, 2018: Remote Sensing Systems SMAP Ocean Surface
801 Salinities [Level 3 Running 8-day], Version 3.0 validated release. Remote Sensing Systems
802 Santa Rosa, CA, USA.
- 803 Munk, W., 1981: Internal waves and small-scale processes, evolution of physical oceanography
804 ba warren, c. wunsch, 264–291. MIT Press, Cambridge, Mass.
- 805 Pinkel, R., M. Buijsman, and J. M. Klymak, 2012: Breaking topographic lee waves in a tidal
806 channel in luzon strait. *Oceanography*, **25** (2), 160–165.
- 807 Polzin, K., and R. Ferrari, 2004: Isopycnal dispersion in natre. *Journal of physical oceanography*,
808 **34** (1), 247–257.
- 809 Prasanna Kumar, S., P. Muraleedharan, T. Prasad, M. Gauns, N. Ramaiah, S. De Souza, S. Sarde-
810 sai, and M. Madhupratap, 2002: Why is the bay of bengal less productive during summer
811 monsoon compared to the arabian sea? *Geophysical Research Letters*, **29** (24), 88–1.
- 812 Prasanna Kumar, S., and Coauthors, 2004: Are eddies nature's trigger to enhance biological pro-
813 ductivity in the bay of bengal? *Geophysical Research Letters*, **31** (7).
- 814 Ramachandran, S., and Coauthors, 2018: Submesoscale processes at shallow salinity fronts in the
815 bay of bengal: Observations during the winter monsoon. *Journal of Physical Oceanography*,
816 **48** (3), 479–509.
- 817 Ruddick, B., and O. Kerr, 2003: Oceanic thermohaline intrusions: Theory. *Progress in Oceanog-*
818 *raphy*, **56** (3-4), 483–497.
- 819 Rudnick, D. L., and S. T. Cole, 2011: On sampling the ocean using underwater gliders. *Journal of*
820 *Geophysical Research: Oceans*, **116** (C8).

- 821 Rudnick, D. L., and J. P. Martin, 2002: On the horizontal density ratio in the upper ocean. *Dynam-*
822 *ics of atmospheres and oceans*, **36** (1-3), 3–21.
- 823 Sarma, V., and T. Udaya Bhaskar, 2018: Ventilation of oxygen to oxygen minimum zone due to
824 anticyclonic eddies in the bay of bengal. *Journal of Geophysical Research: Biogeosciences*,
825 **123** (7), 2145–2153.
- 826 Schmidtko, S., G. C. Johnson, and J. M. Lyman, 2013: MIMOC: A global monthly isopycnal
827 upper-ocean climatology with mixed layers. *Journal of Geophysical Research: Oceans*, **118** (4),
828 1658–1672.
- 829 Sengupta, D., G. Bharath Raj, and S. Shenoi, 2006: Surface freshwater from Bay of Bengal runoff
830 and Indonesian throughflow in the tropical Indian Ocean. *Geophysical Research Letters*, **33** (22).
- 831 Shcherbina, A. Y., and Coauthors, 2015: The LatMix summer campaign: Submesoscale stirring
832 in the upper ocean. *Bulletin of the American Meteorological Society*, **96** (8), 1257–1279.
- 833 Shetye, S., S. Shenoi, A. Gouveia, G. Michael, D. Sundar, and G. Nampoothiri, 1991: Wind-
834 driven coastal upwelling along the western boundary of the bay of bengal during the southwest
835 monsoon. *Continental Shelf Research*, **11** (11), 1397–1408.
- 836 Shroyer, E., and Coauthors, 2019: Upper layer thermohaline structure of the bay of bengal during
837 the 2013 northeast monsoon. *Deep Sea Research Part II: Topical Studies in Oceanography*,
838 104630.
- 839 Shroyer, E. L., D. L. Rudnick, J. T. Farrar, B. Lim, S. K. Venayagamoorthy, L. C. St. Laurent,
840 A. Garanaik, and J. N. Moum, 2016: Modification of upper-ocean temperature structure by
841 subsurface mixing in the presence of strong salinity stratification. *Oceanography*, **29** (2), 62–
842 71.

- 843 Siegelman, L., P. Klein, P. Rivière, A. F. Thompson, H. S. Torres, M. Flexas, and D. Menemenlis,
844 2020: Enhanced upward heat transport at deep submesoscale ocean fronts. *Nature Geoscience*,
845 **13** (1), 50–55.
- 846 Smith, K. S., and R. Ferrari, 2009: The production and dissipation of compensated thermohaline
847 variance by mesoscale stirring. *Journal of Physical Oceanography*, **39** (10), 2477–2501.
- 848 Sundermeyer, M. A., and J. R. Ledwell, 2001: Lateral dispersion over the continental shelf: Anal-
849 ysis of dye release experiments. *Journal of Geophysical Research: Oceans*, **106** (C5), 9603–
850 9621.
- 851 Sundermeyer, M. A., J. R. Ledwell, N. S. Oakey, and B. J. Greenan, 2005: Stirring by small-scale
852 vortices caused by patchy mixing. *Journal of Physical Oceanography*, **35** (7), 1245–1262.
- 853 Thomas, L. N., and C. J. Shakespeare, 2015: A new mechanism for mode water formation involv-
854 ing cabbeling and frontogenetic strain at thermohaline fronts. *Journal of Physical Oceanogra-*
855 *phy*, **45** (9), 2444–2456.
- 856 Thomas, L. N., A. Tandon, and A. Mahadevan, 2008: Submesoscale processes and dynamics.
857 *Ocean modeling in an Eddying Regime*, **177**, 17–38.
- 858 Thompson, A. F., A. Lazar, C. Buckingham, A. C. Naveira Garabato, G. M. Damerell, and K. J.
859 Heywood, 2016: Open-ocean submesoscale motions: A full seasonal cycle of mixed layer in-
860 stabilities from gliders. *Journal of Physical Oceanography*, **46** (4), 1285–1307.
- 861 Thomson, R. E., and W. J. Emery, 2014: *Data Analysis Methods in Physical Oceanography*.
862 Newnes.
- 863 Vallis, G. K., 2017: *Atmospheric and Oceanic Fluid Dynamics*. Cambridge University Press.

- 864 Woods, O. R., J., and J. Fischer, 1986: Thermohaline intrusions created isopycnically at oceanic
865 fronts are inclined to isopycnals. *Nature*, **322**, 446–449.
- 866 Yi-Neng, L., P. Shi-Qiu, and Z. Xue-Zhi, 2012: Observations and simulations of the circulation
867 and mixing around the andaman-nicobar submarine ridge. *Atmospheric and Oceanic Science*
868 *Letters*, **5** (4), 319–323.
- 869 Young, W., P. Rhines, and C. Garrett, 1982: Shear-flow dispersion, internal waves and horizontal
870 mixing in the ocean. *Journal of Physical Oceanography*, **12** (6), 515–527.
- 871 Yu, X., A. C. Naveira Garabato, A. P. Martin, C. E. Buckingham, L. Brannigan, and Z. Su, 2019:
872 An annual cycle of submesoscale vertical flow and restratification in the upper ocean. *Journal*
873 *of Physical Oceanography*, **49** (6), 1439–1461.

874 LIST OF FIGURES

875 Fig. 1.	Schematic of spectral distributions of passive tracer	41
876 Fig. 2.	The Bay of Bengal's surface salinity and subsurface oxygen saturation	42
877 Fig. 3.	Tracks of 3 cruises, currents, and climatological spice	43
878 Fig. 4.	Vertical profiles of temperature, salinity, and stratification	44
879 Fig. 5.	Depth and stratification of isopycnals	45
880 Fig. 6.	Density vs. distance sections of spice from cruises in the Bay of Bengal	46
881 Fig. 7.	Salinity along all sections on $\sigma = 22$ and 25 isopycnals.	47
882 Fig. 8.	Individual spectral estimates, frequency-bin averaged, along all sections	48
883 Fig. 9.	Individual spectral slope estimates along all sections	49
884 Fig. 10.	Comparison of tracer variance wavenumber spectra at different depths	50
885 Fig. 11.	Global map of eddy kinetic energy with locations of isopycnal spice studies	51
886 Fig. 12.	Schematic of the observed change in spectral slope of spice variance	52
887 Fig. 13.	Strong submesoscale density fronts in the surface mixed layer	53

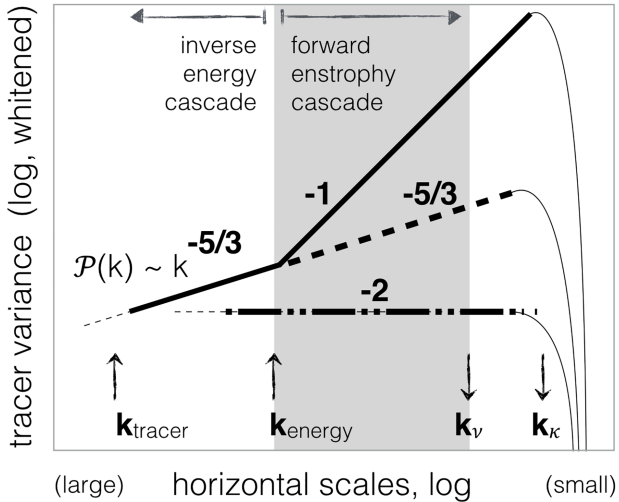
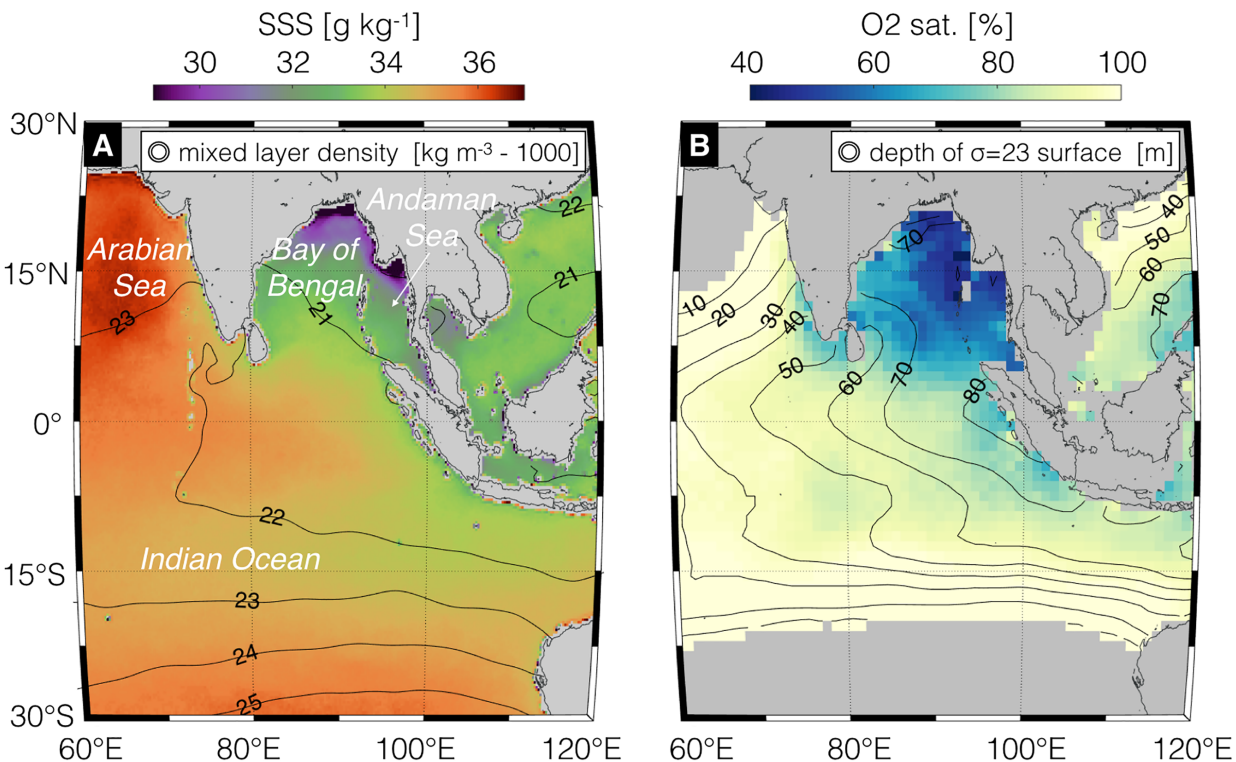


FIG. 1. Schematic of passive tracer spectral distributions $\mathcal{P}(k)$, whitened (multiplied by $4\pi^2 k^2$) for clarity of presentation, and shown on log-log axes. Predictions of spectral shapes of a tracer stirred by 2-dimensional homogeneous turbulence, according to several theories: interior QG (blue), surface QG (orange), stratified “pancake” turbulence (orange), and frontogenesis (magenta). These predictions assume tracer variance in the ocean is introduced at the large scale (wavenumber k_{tracer}), cascades to smaller scales by the 2-dimensional macro-turbulence, and is destroyed by 3-dimensional isotropic turbulent mixing. Energy is assumed to be injected at an intermediate scale (k_{energy}) and cascades to larger scales in QG theory, producing a break in the predicted slope between the inverse energy cascade regime (where the kinetic energy spectrum $\mathcal{E}(k) \sim k^{-5/3}$, not shown), and the forward enstrophy cascade regime (where $\mathcal{E}(k) \sim k^{-3}$). While energy falls off rapidly in the viscous inertial regime (wavenumber larger than k_v), passive tracer variance does not fall off until the diffusive regime (wavenumber larger than k_k).



899 FIG. 2. Freshwater inputs lower the Bay of Bengal's surface salinity and strongly stratify the upper ocean,
900 insulating a pronounced oxygen minimum zone (OMZ) below about 75 m depth. **(A)** Average surface salinity
901 in 2017, measured by NASA's SMAP (Soil Moisture Active Passive) mission (Meissner et al. 2018). Contoured
902 is climatological annual mixed layer density, from MIMOC (Schmidtko et al. 2013). **(B)** Climatological oxygen
903 saturation at 1023 kg m^{-3} density ($\sigma = 23$) from WOCE. Contoured is the depth of the 1023 kg m^{-3} surface.
904 At a mean depth of about 75 m in the Bay of Bengal, this density surface does not regularly outcrop in the bay.
905 Low biological productivity compared to other OMZ regions suggest that the subsurface waters in the Bay of
906 Bengal have long residence-times with little ventilation.

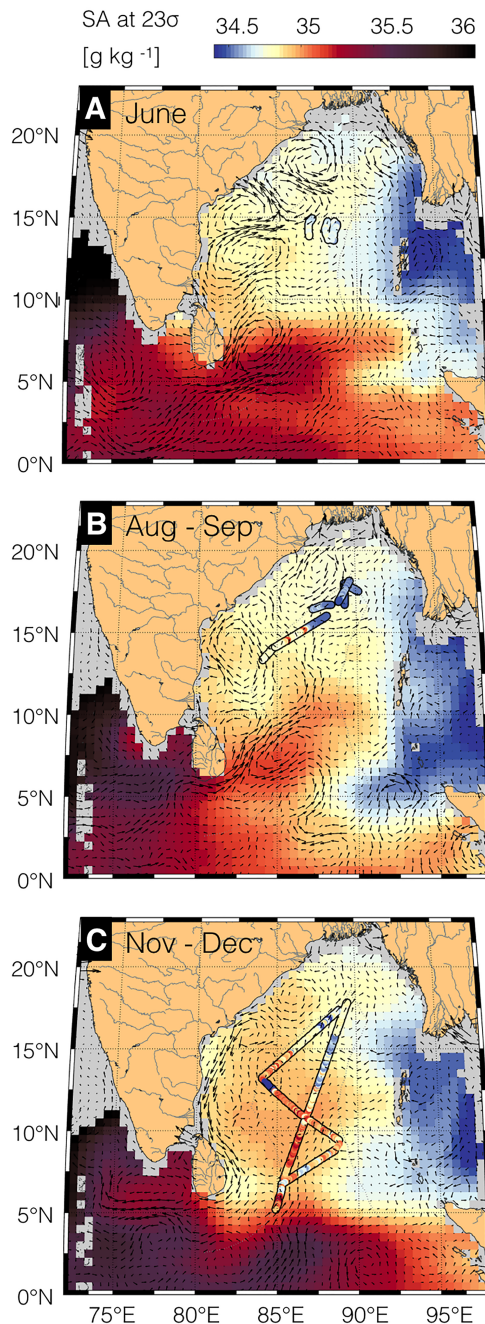


FIG. 3. The three research expeditions' tracks and the mesoscale currents at the time, along with climatological spice patterns. (A) 6-18th June 2018, (B) 24th August - 20th September 2015, (C) 29th November - 11th December 2013. Background colors show the climatological salinity on the $\sigma = 23$ surface for each respective month(s) from MIMOC. The colored dots show the ship-observed salinity at the same density, for all sections longer than 100 km. The black arrows show surface AVISO currents for a particular time period during each cruise. The basin-scale spice gradient is between salty-warm water from the Arabian Sea and relatively fresh-cold water, in the Andaman Sea. The western side of the Bay of Bengal hosts energetic mesoscale eddies of $O(100)$ km scale, as well as seasonally reversing boundary currents.
44

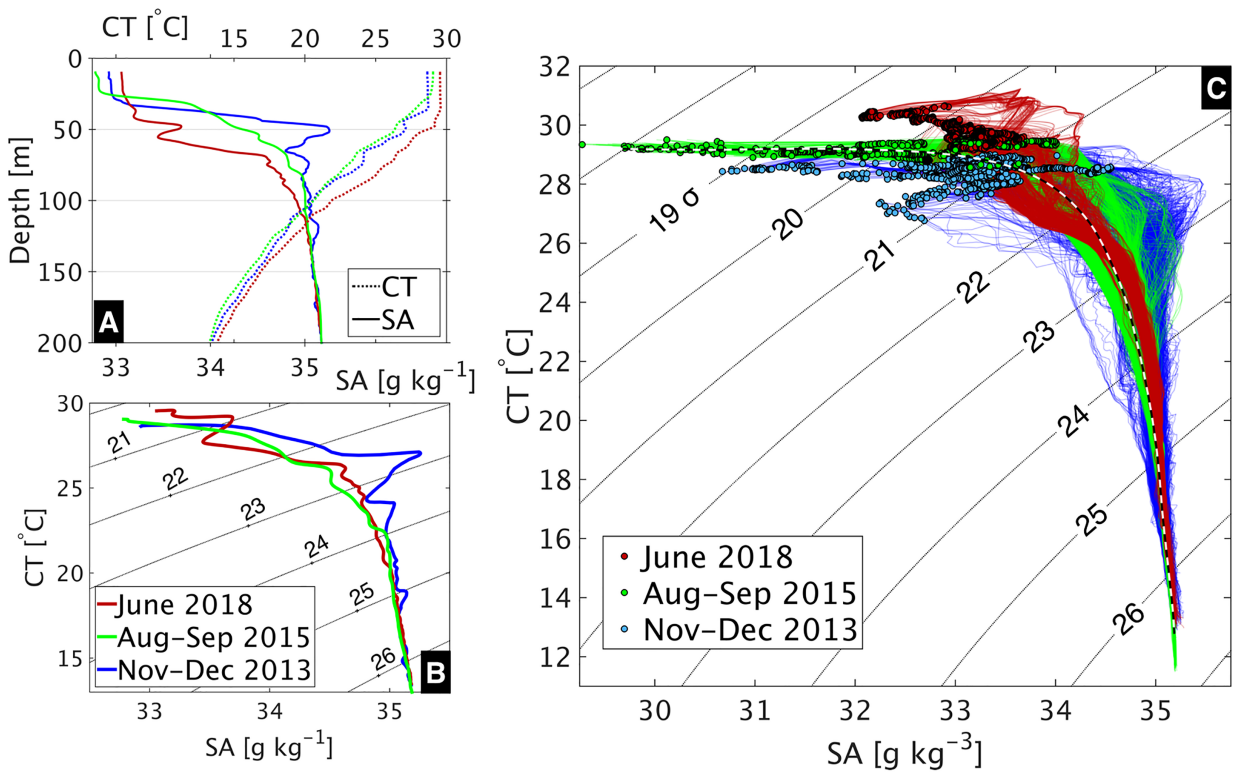


FIG. 4. The Bay of Bengal's upper ocean is characterized by a shallow sharp halocline above a deeper thermocline creating strong density stratification, and a subsurface layer of enhanced water mass variability. (A) Example profiles of Absolute Salinity (solid) and Conservative Temperature (dashed) from each cruise: June 2018 (red), August–September 2015 (green), Nov–Dec 2013 (blue). The vertical resolution of profiles is at least 1m. (B) Corresponding *TS* profiles. Thin curved contours show potential density referenced to the surface. (C) Plot of *TS* profiles measured on all 3 cruises. Circles mark surface mixed layer values. The dashed black-white line is a smoothed median *TS* profile from all cruises, used as the reference for calculating along-isopycnal spice (spicy and minty).

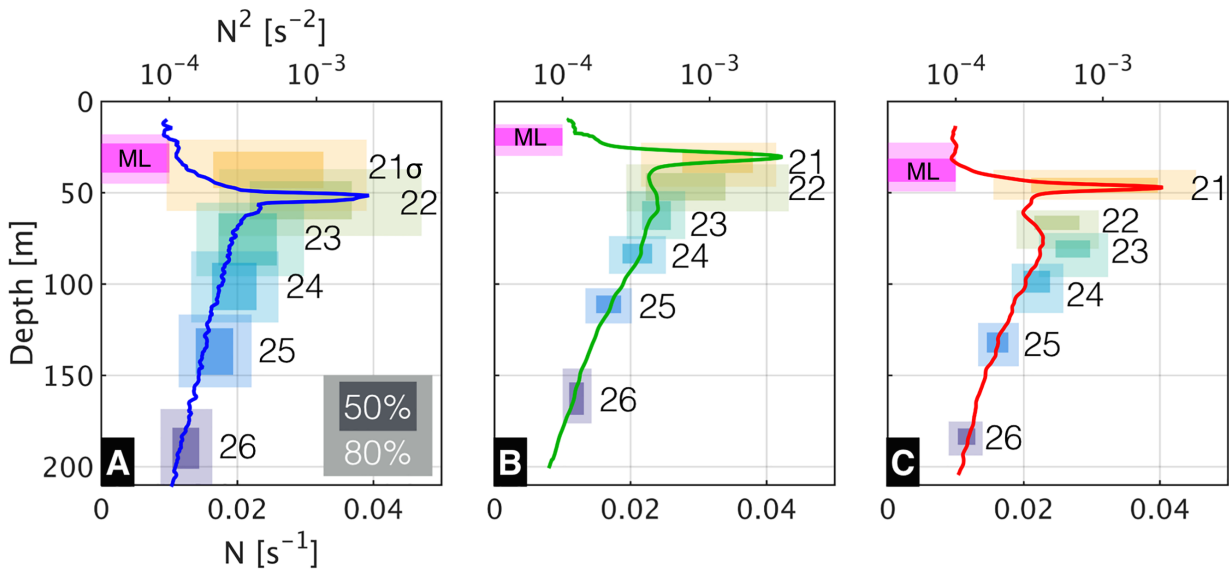
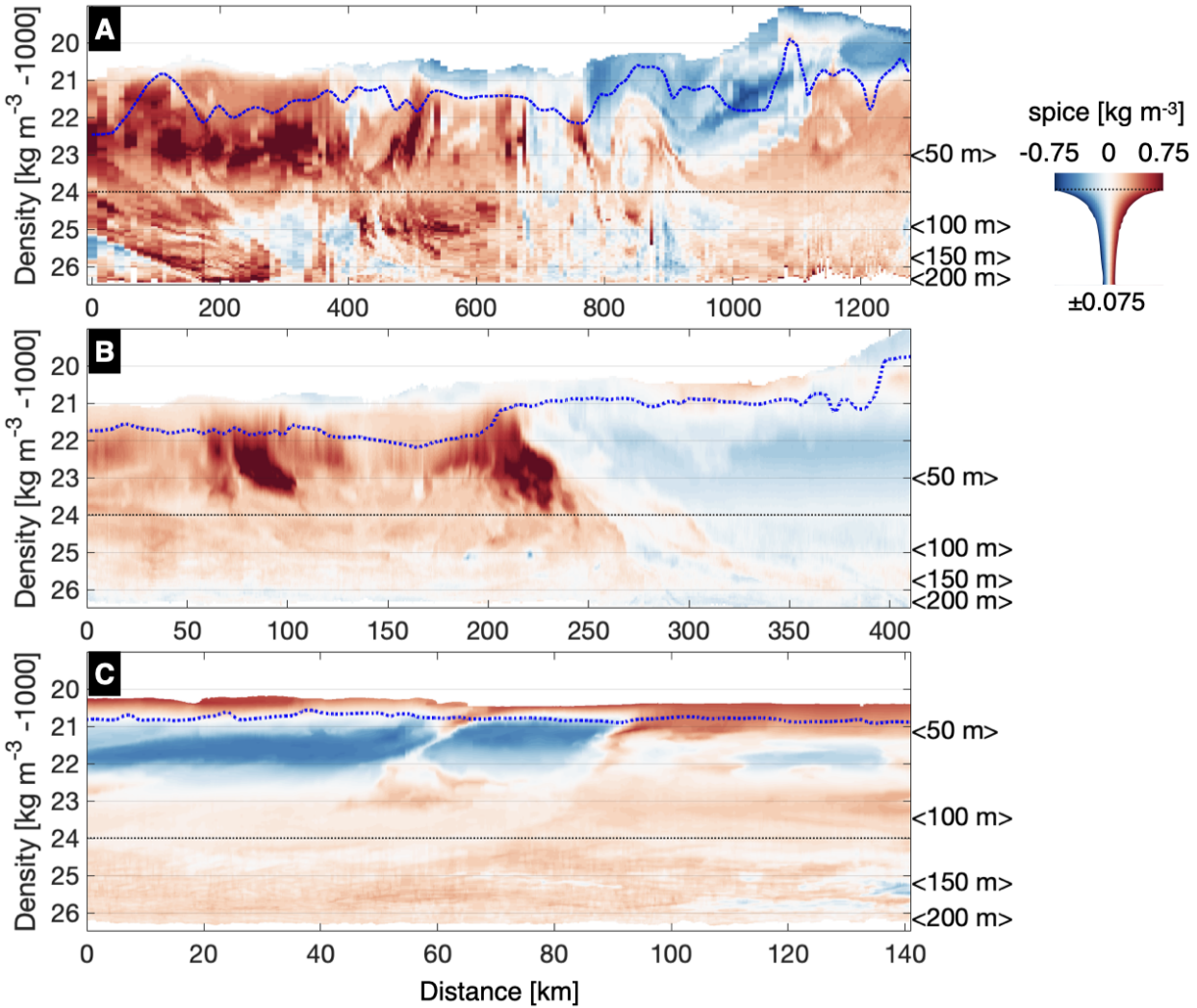
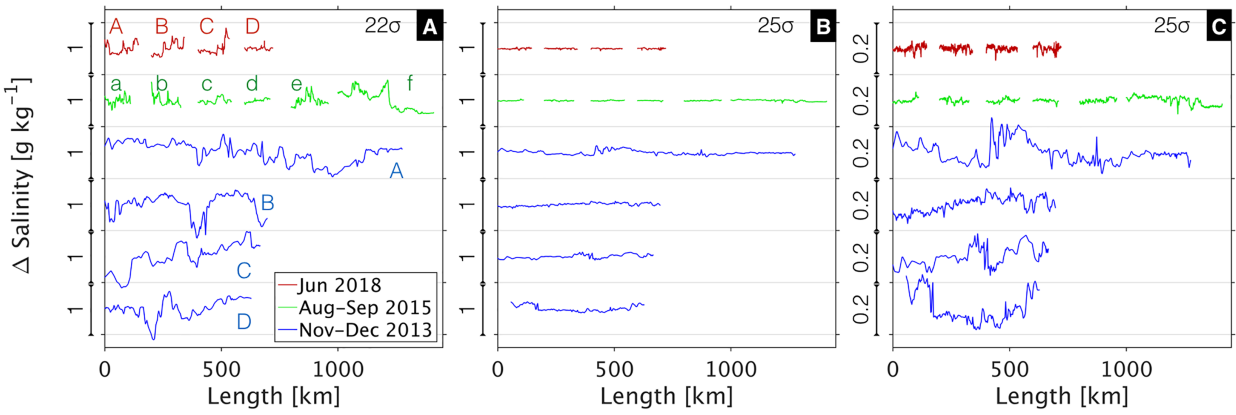


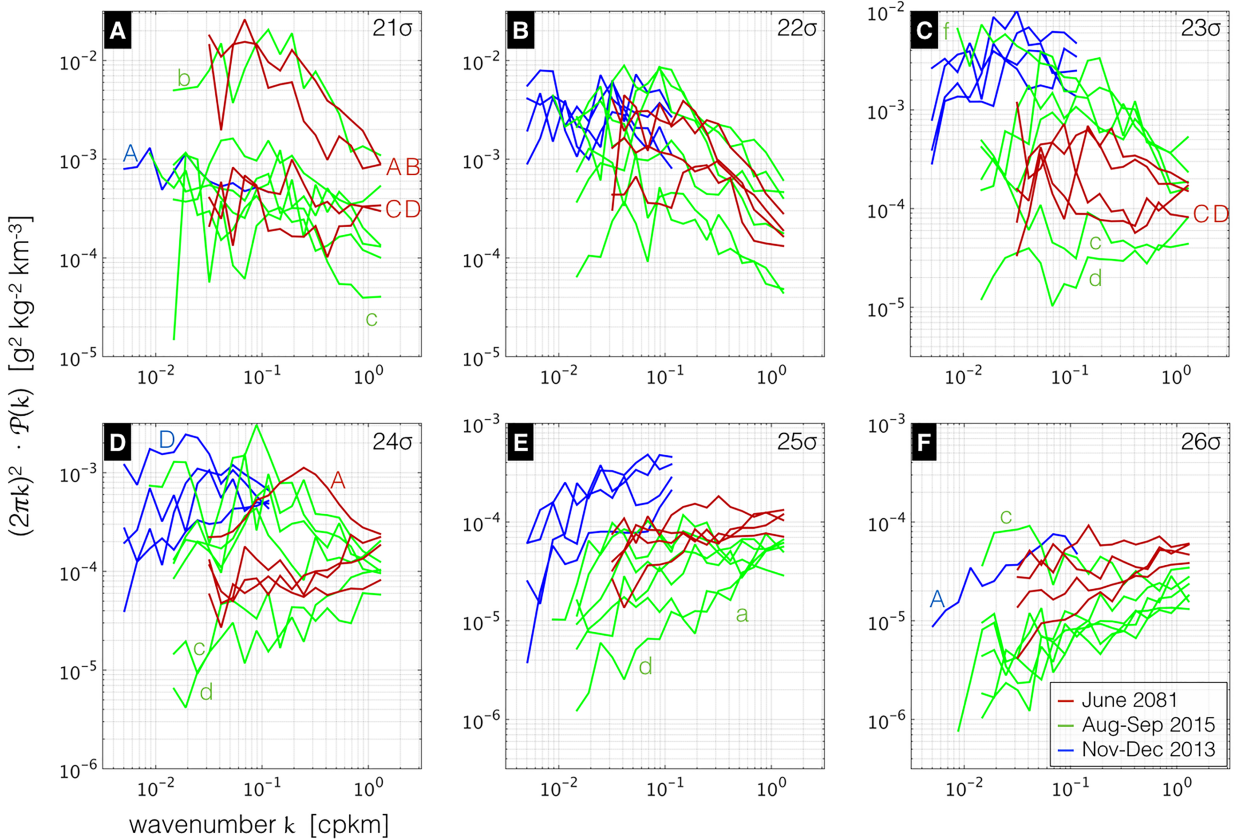
FIG. 5. Solid lines show the mean density stratification profiles. (A) Nov.-Dec. 2013 (B) Aug.-Sep. 2015 (C) June 2018. To preserve the sharpness of the typical individual stratification profile, the average is calculated by first vertically shifting all individual profiles, such that their peaks align at the average depth of maximum stratification (average density level of peak N^2 : (2013) 21.9, (2015) 20.7, (2018) 21.1). Shaded boxes show the distribution of depth and stratification at the isopycnal levels 21 to 26 σ (yellow to blue) during the 3 hydrographic surveys. The darker box covers the interquartile range of values, the lighter box covers the 10th to 90th percentile of values. Similarly shown is the range of depth of the mixed layer (magenta).



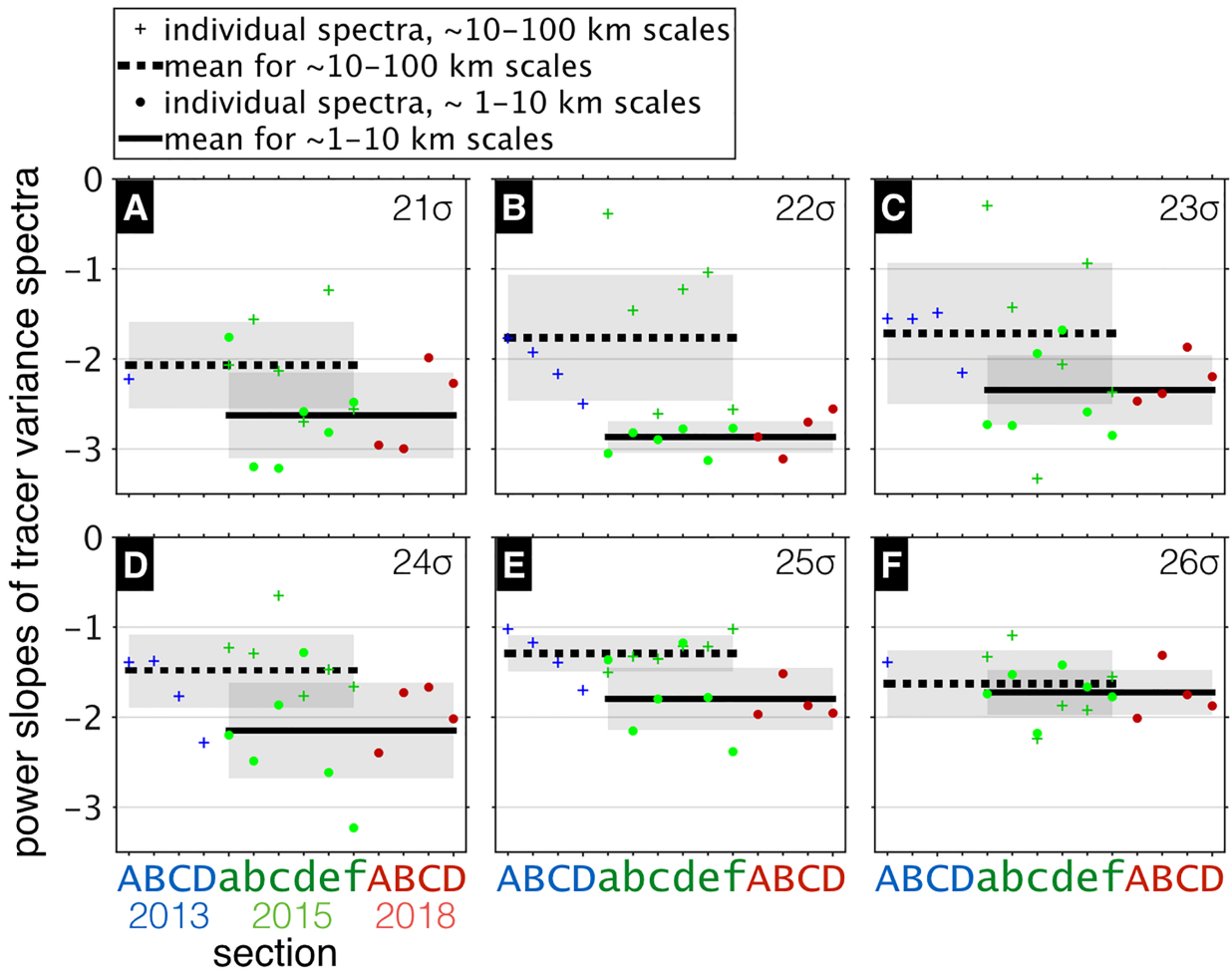
930 FIG. 6. Density vs. distance sections of spice from cruises in the Bay of Bengal in (A) 2013, (B) 2015,
 931 and (C) 2018. Note the different horizontal scales. Spice (red = warm & salty, blue = cold & fresh) is defined
 932 as $\alpha\Delta T + \beta\Delta S$, the along-isopycnal density-compensated TS anomaly from the reference TS profile shown in
 933 Fig.4C. Note that below the $\sigma = 24$ isopycnal (dotted line), the color values have been enhanced by a factor of
 934 up to 10, as indicated in the colorbar, to show the spice anomalies at depth that are an order of magnitude smaller
 935 than the shallower anomalies. Blue dashed line marks the density of maximum stratification N^2 . On the right
 936 vertical axis are marked the isopycnal levels with average depths of 50, 100, 150, and 200 m.



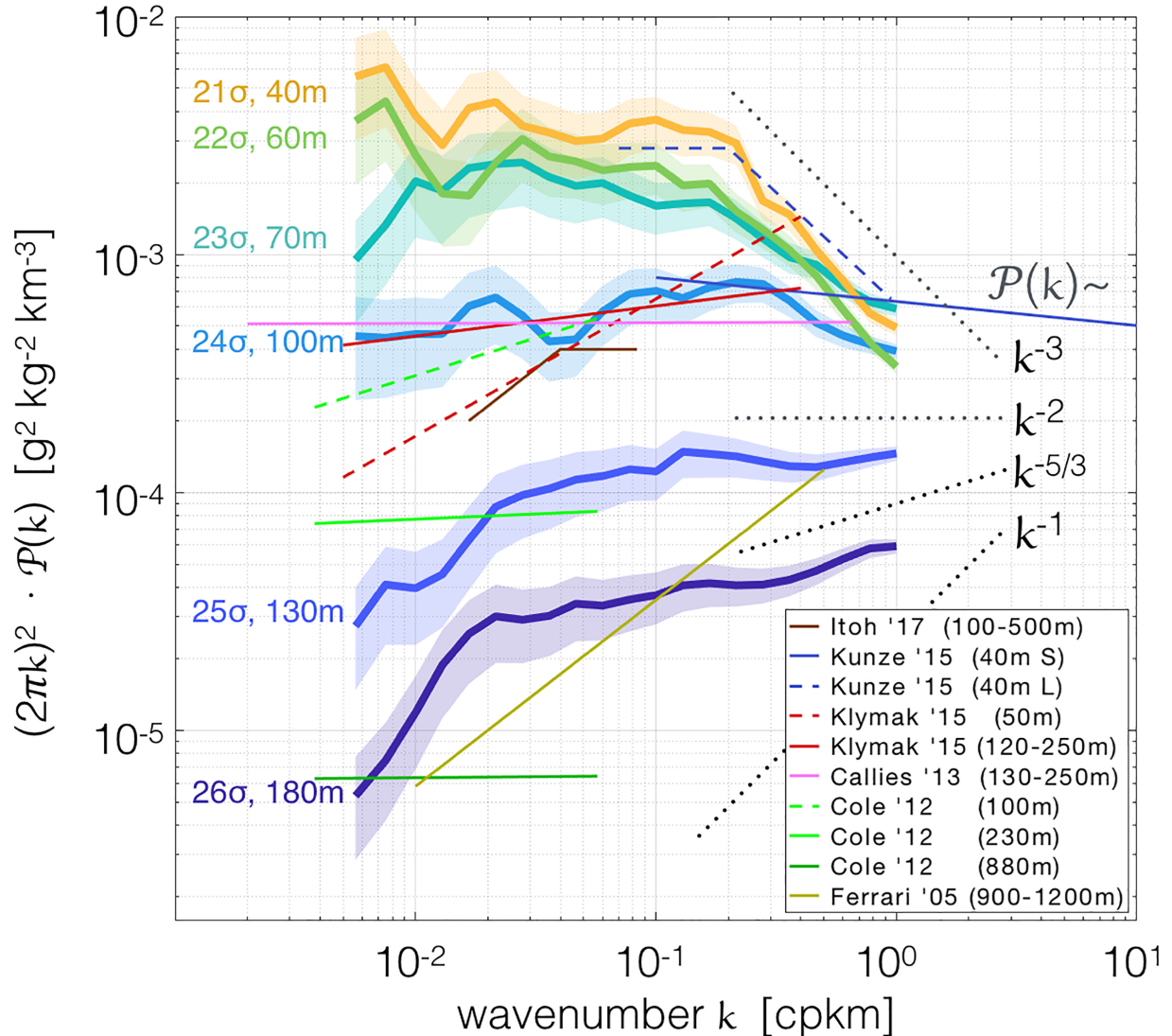
937 FIG. 7. Salinity (relative values, vertically offset) along all sections on (A) $\sigma = 22$ and (B-C) $\sigma = 25$ isopyc-
 938 nals. All sections longer than 100 km (labeled A to F, shown in Supp. Fig.S2) from the 2018 (red), 2015 (green)
 939 and 2013 (blue) cruises. The vertical scale of panel (C) is reduced by a factor of 5 to show the weaker salinity
 940 fluctuations along this deeper isopycnal.



941 FIG. 8. Individual spectral estimates, frequency-bin averaged, along all sections longer than 100 km (partic-
942 ular letter-labels refer to Supp. Fig. S2) during all cruises (red = 2018, green = 2015, blue = 2013), along the
943 same isopycnals ($\sigma = 21$ to 26).



944 FIG. 9. Individual spectral slope estimates of all spectra in Fig.8 for isopycnals $\sigma = 21$ to 26. The crosses
 945 (blue = 2013, green = 2015) mark the spectral slope between scales of $O(100 - 10)$ km, the circles (green =
 946 2015, red = 2018) between scales of $O(10 - 1)$ km. The black lines mark the average slope over these two scale
 947 ranges, shaded in gray is the standard deviation.



948 FIG. 10. Comparison of horizontal wavenumber variance spectra for salinity anomalies along isopycnals at
949 different mean depths, from the Bay of Bengal (shaded areas represent confidence bound estimates as described
950 in text). Thin straight lines depict spectra from other published studies: the CUGN project in the California
951 Current System (Itoh and Rudnick 2017), the LatMix project in the Atlantic's Sargasso Sea (Kunze et al. 2015)
952 and the NATRE project in the subtropical Atlantic (Ferrari and Polzin 2005), the Line P and IWAP cruises
953 (Klymak et al. 2015), the Spice dataset (Callies and Ferrari 2013), and data from gliders (Cole and Rudnick 2012)
954 in the subtropical and northern Pacific. Lines are graphical best-fits of the slopes, converted to salinity anomaly
955 spectra in wavenumber k (cycles per kilometer) multiplied by $4\pi^2 k^2$. Dotted gray lines mark the whitened slopes
956 of variance spectra $\mathcal{P}(k) \sim k^m$ with power laws of $m = -1$ (QG stirring), $-5/3$ (SQG / Obukhov-Corrsin), -2
957 (frontogenesis), and the observed decay of -3 of the shallow BoB spectra below $O(10)$ km.

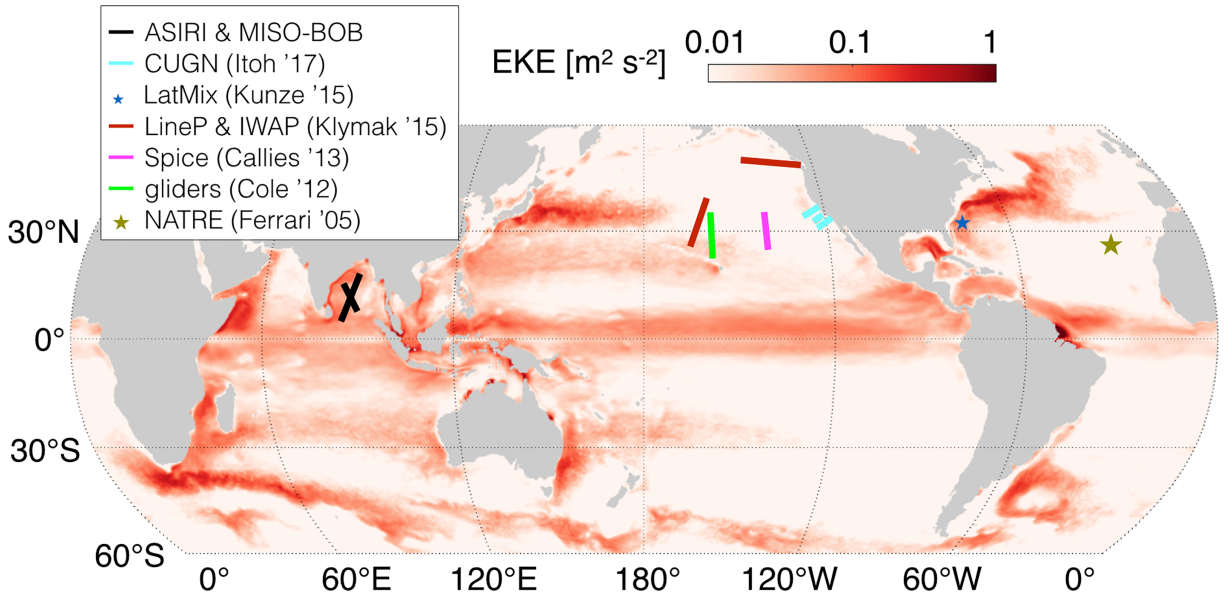
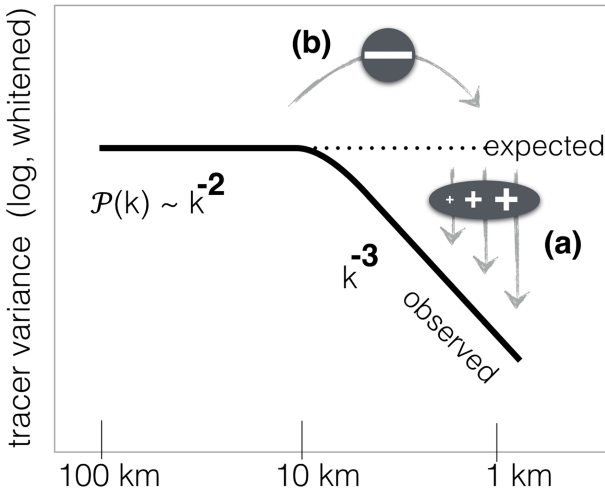
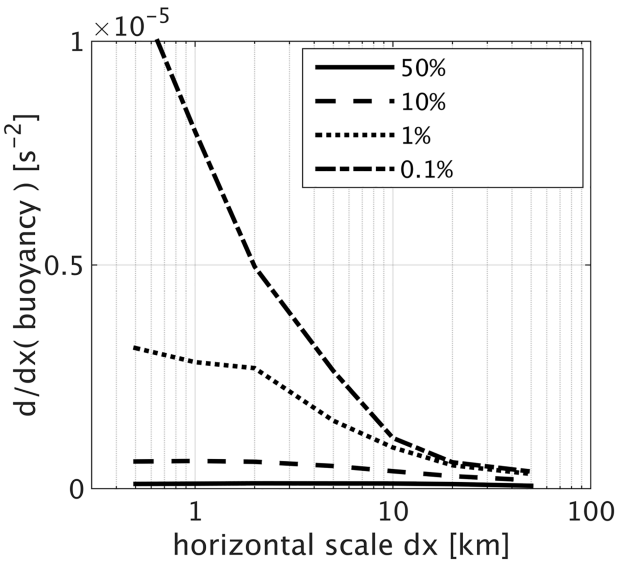


FIG. 11. Global map of eddy kinetic energy $= \frac{1}{2}(u'^2 + v'^2)$ based on daily 0.25° fields from the Global Ocean
 Gridded SSALTO/DUACS Sea Surface Height L4 product averaged from 2013 to 2017. Colored lines and stars
 show the location of studies reporting along-isopycnal salinity or temperature spectra, shown in Fig.10. Note
 that only the LatMix study in the Western Atlantic (blue star) was located in a similarly energetic region as the
 Bay of Bengal (black line).



963 FIG. 12. Representation of the observed change in spectral slope of spice variance $\mathcal{P}(k)$ (whitened) along
 964 the shallower isopycnals in the BoB, idealized from Fig.10. Given the variance present at scales $O(10)$ km,
 965 we expect at least the same (whitened) variance level to be seen at smaller scales (dotted line), given any of
 966 the theories of 2-dimensional stirring in a statistical steady-state. Two potential explanations are suggested
 967 for the increasing deficit of tracer variance below 10 km scales. Either (a) the $O(1)$ km horizontal variance
 968 is destroyed by vertical mixing that is effectively felt at this horizontal scale, which is much larger than the
 969 3-dimensional isotropic mixing scale. Potential candidates are shear dispersion or submesoscale instabilities.
 970 Or (b) the down-scale cascade of variance from larger scales is inhibited beyond ~ 10 km scales in the Bay of
 971 Bengal. A potential reason could be coherence between spice anomalies and dynamic anomalies, such that spice
 972 spectral distributions do not reflect stirring by homogeneous macro-turbulence of an independent, stochastically
 973 distributed tracer, but rather the distribution of a dynamically relevant property.



974 FIG. 13. The Bay of Bengal's surface mixed layer contains strong submesoscale density fronts. Magnitudes
 975 of buoyancy gradients $|\frac{g}{\rho_0} \frac{d}{dx} \rho|$ are calculated along the horizontal sections longer than 100 km from the 2015
 976 survey, and low-pass filtered (3rd order Butterworth) with increasingly larger cut-off wavelengths. Colored lines
 977 show the top percentiles (0.1, 1, 10, and 50%) of the buoyancy gradients, showing that the strongest fronts have
 978 widths below $O(1)$ km, and are at least one order of magnitude stronger than mesoscale gradients.